

Characterization of the Structure in Asphalts by Employing X-Ray Technique

By

Haytem Geneve

Submitted to

The School of Graduate Studies

in partial fulfillment of the requirements for the degree of

**Master of Engineering**

Faculty of Engineering and Applied Science

Memorial University of Newfoundland

November 2017

St. John's

Newfoundland

Canada

## Abstract

Asphalt binder of five samples were taken from different parts of Canada. Thin films samples (1 mm) were prepared by heating onto glass slides at 150°C for 10 min. Structural studies of asphalt in crude oil were performed by X-ray diffraction (XRD). The Jade™ software program was used for the initial analysis. XRD was performed with copper K- $\alpha$  radiation at 40 kV and 40 mA at a scan rate of 0.001° 2 $\theta$  per second. The XRD data were first fitted with the Pearson VII features and then with pseudo-Voigt features and then modeled in the Mathematica© using the Fermi Generalized Function (GFF). The results are discussed in terms of their accuracy with different combinations of backgrounds such as (Linear, Level, Fixed, Parabolic, 3rd order Polynomial, 4th order Polynomial).

The outcomes discussed are related to the accuracy of profile fitting when the exponents of Pearson VII and pseudo- Voigt Lorentzian differ. The Lorentzian values of Pseudo- Voigt are 0.4, 0.7, and 0.9 whereas the Exponent values of Pearson VII are 0.6, 0.8, and 1.2, and 3 backgrounds (4th order polynomial, 3rd order polynomial, and parabolic) were applied in profile fitting. Further, profile fitting and accuracy extend to crystallite parameters calculated results.

## **Acknowledgements**

Primarily, I would like to sincerely thank my supervisors Dr. John Shirokoff and Dr. John Lewis for their encouragement, guidance, and most importantly, their friendship during my graduate studies at Memorial University. For everything you have done for me, Dr. John Shirokoff and Dr. John Lewis, I thank you. Finally, and most importantly, I would like to thank my parents for their support and encouragement.

## Table of Contents

Abstract.....	ii
Acknowledgements.....	iii
List of Tables .....	vii
List of Figures.....	viii
Abbreviations list.....	xi
Symbols List .....	xii
Chapter 1.....	1
1.1 Introduction.....	1
1.2 Types of Asphalt.....	2
1.2.1 Hot Mix Asphalt (HMA) .....	3
1.2.1.1 Hot mix asphalt: Density mixture.....	3
1.2.1.2 Hot mix asphalt: Stone asphalt matrix .....	3
1.2.1.3 Hot mix asphalt: Open-graded mixes .....	4
1.2.2 Cold mix asphalt (CMA) .....	4
1.2.3 Petroleum Asphaltene .....	5
1.2.4 Asphalt Cement .....	6
1.3 PG and PBA Binder.....	6
1.4 Crude Oil Characterization .....	7
1.4.1 Asphaltenes.....	10
1.4.2 Molecular Structure .....	12
1.4.3 Density.....	14
1.4.4 Surface Activity.....	14
1.5 Asphalt Physical Properties .....	16
1.6 X-ray Diffraction (XRD).....	17
1.7 Bragg's Diffraction.....	19
1.8 Objectives of the Research .....	21
Chapter 2.....	22

2.1 Internal Structure of Asphalt .....	22
2.2 Self-Association and Molar Mass.....	24
2.3 SAXS and SANS .....	25
2.4 X-ray Spectral Line Shape Analysis of Asphalt Binders.....	26
2.5 Aging of Asphalt Binder.....	29
2.6 XRD .....	30
2.7 Modeling Asphalt as a Cubic Material (Yen Model) .....	32
2.8 Modified Yen model (the Yen-Mullins model).....	33
2.9 Asphalt Chemical Components and Modification Efforts.....	34
2.10 Low Temperature and Fatigue Cracking in Asphalt Pavement.....	35
2.11 Morphological Characterization .....	38
Chapter 3.....	39
3.1 Instrument and Measuring Principle.....	39
3.2 Demonstration of X-ray Diffraction .....	39
3.3 Sample Preparation for XRD.....	45
3.4 Method of Thin Film XRD .....	46
3.5 Instruments for X-ray Thin-Film Measurements.....	47
3.6 Spectral Line Shapes Modeling Using Mathematical Functions.....	48
3.7 Line Shape Analysis Using Peak Search and Profile Fit .....	48
Chapter 4.....	49
4.1 XRD Patterns .....	49
4.2 XRD Types with Different Backgrounds and Effect of Backgrounds .....	54
4.3 Peak Shape Functions .....	55

4.4 Samples Figures with GFF .....	60
4.5 Comparing the Results of all Asphalt Samples .....	63
Chapter 5.....	71
Conclusion .....	71
Recommendations for Future Work .....	72
References.....	73

## List of Tables

Table 1. 1 Classification of Crude Oils .....	8
Table 1. 2 Elemental Composition of Various Asphaltenes .....	12
Table 3. 1 Pertinent Asphalt Binder Properties .....	45
Table 4.1 The Aromaticity and Crystallite Parameters Calculated with The Use of Pearson VII, Pseudo-Voigt, and GFF.....	64
Table 4.2 The Aromaticity and Crystallite Parameters Calculated with the Use of Pearson VII, Pseudo-Voigt, and GFF.....	65

## List of Figures

Figuier 1.1 Continuum of Saturates, Aromatics, Resins and Asphaltenes (Sara) in Petroleum [13]. .....	10
Figuier 1.2 Model of asphaltene molecules: a) the “continental” type, and b) the “archipelago” type [14].....	13
Figuier 1.3 A schematic illustration of X-ray diffraction by a crystal [32]. .....	20
Figure 2.1: The cross section of asphaltene cluster structure model [47] .....	28
Figure 2.2 Means profiles from CAP 50/70 by REPAR Refinery in each time [55]. ....	31
Figure 2. 3 The Yen–Mullins Model [57] .....	32
Figure 2. 4 (A) Xrd Pattern of Asphaltene, (B) Planes Corresponding to The Peaks in The Xrd Pattern [58].....	34
Figure 2. 5 Alligator-type fatigue cracks typically due to load (traffic) distress [67].....	36
Figure 2.6 Longitudinal and transverse cracks typically due to thermal effects [67].....	37
Figure 3. 1 Reflection of x-rays in the (hkl) planes of a crystal [32]. .....	41
Figure 3.2 Geometric arrangement of X-ray diffractometer [72].....	42
Figure 3.3 X-ray thin-film diffractometer equipped with a $2\Theta$ $\chi$ axis (SmartLab) [76].....	47
Figure 4.1a: Specimen L3 (4 <sup>th</sup> order background, Lorentzian =0.4) . .....	49
Figure 4.21b: Specimen L3 (parabolic background, Lorentzian =0.7).....	50

Figure 4.2 Specimen L3 (4 <sup>th</sup> Order Background, Lorentzian =0.4) and L3 of XRD (Parabolic Background, Lorentzian =0.7).....	50
Figure 4. 3 Specimen L5 (3 <sup>rd</sup> Order Background, Lorentzian =0.9) and L5 of XRD (3 <sup>rd</sup> Order Background, Lorentzian, Lorentzian =0.9).....	<u>51</u>
Figure 4. 4 Specimen 655-1 (4 <sup>th</sup> Order Background, Lorentzian =0.9) and 655-1 of XRD (Parabolic Background, Lorentzian, Lorentzian =0.4).....	51
Figure 4. 5 Specimen L6 (Parabolic Background, Lorentzian, Lorentzian =0.9). and L6 of XRD (4 <sup>th</sup> Order Background, Lorentzian =0.4).....	52
Figure 4. 6 Specimen L7 (3 <sup>rd</sup> Order Background, Lorentzian =0.9) and L7 of XRD (4 <sup>th</sup> Order Background, Lorentzian =0.4). ....	53
Figure 4. 7 Gauss and Lorentz Peak Shape Functions [48].....	58
Figure 4. 8 Sample L3 From GFF. ....	61
Figure 4. 9 Sample L5 From GFF .....	61
Figure 4. 10 Sample L6 From GFF. ....	62
Figure 4. 11 Sample L7 From GFF. ....	62
Figure 4. 12 Aromaticity and Crystallite Parameters Sample L3 Calculated Using Pearson Vii, Pseudo-Voigt and 4 <sup>th</sup> - Order Background.....	67
Figure 4. 13 Aromaticity and Crystallite Parameters Sample L5 Calculated Using Pearson Vii, Pseudo-Voigt and Gff Parabolic Background.....	68
Figure 4. 14 Aromaticity and Crystallite Parameters Sample L6 Calculated Using Pearson Vii, Pseudo-Voigt and Gff 4 <sup>th</sup> -Order Background. ....	68
Figure 4. 15 Aromaticity and Crystallite Parameters Sample L7 Calculated Using, Pseudo-Voigt And 3 <sup>rd</sup> -Order Background. ....	69

Figure 4.16 Modified figure of relationship showing crystalline dimension  
(vertical) versus bandwidth (horizontal) [48]..... 70

### Abbreviations list

X-ray Diffraction	XRD
Pearson VII	P
Pseudo – Voigt	V
Generalized Fermi Function	GFF
Full-Width Half Maximum	FWHM
Hot Mix Asphalt	HMA
Cold Mix Asphalt	CMA
Performance Grade	PG
Performance Based Asphalt	PBA
United Nations Institute for Training and Research	UNITAR
American Petroleum Institute	API
Asphalt Cement	AC
Aged Residue	AR
American Association of State and Highway Transportation Officials	AASHTO
American Society for Testing and Materials	ASTM
Strategic Highway Research Program	SHRP
Pressure Aging Vessel	PAV
Scatter Slit	SS
Styrene-Butadiene-Styrene	SBS

## Symbols List

$\text{CH}_4$

Methane

$\text{C}_2\text{H}_6$

Ethane

$\text{C}_3\text{H}_8$

Propane

$\text{O}_2$

Oxygen

## Chapter 1

### 1.1 Introduction

Asphalt is a mixture of aggregates, binder and filler, used for constructing and maintaining all kinds of roads, air ports, parking areas, etc. Typical asphalt mixtures are aggregates of crushed rock, sand and gravel. In one of its forms, it has several mixtures of hydrocarbons called bitumen. Asphalt binder is a powerful, versatile weather-resistant chemical binding that adapts itself to a variety of uses. It connects crushed stone and gravel (commonly known as aggregates) in hard surfaces, roads, streets, and airport operation routes. Asphalt is obtained either from natural sediments such as native asphalt or as a by-product of the petroleum industry (petroleum asphalt) [1].

Asphalt is one of the oldest engineering materials in the world, having been used since the beginning of known civilization, around 6000 BC. As early as 2600 BC, the Egyptians used asphalt as waterproofing. In many ancient civilizations, asphalt was widely used as a mortar for building and paving blocks used in temples, irrigation systems, reservoirs, and highways.

The asphalt utilized by early civilizations occurred naturally and was found in geological strata either as soft mortar or hard black veins, which were embedded in brittle rock formations (also known as asphalt charcoal). Natural asphalt was formed when the crude oils were working their way through the cracks of the surface of the earth. The work of the sun and wind removed oil and light gases, leaving black residues. The discovery of asphalt during the refining of crude oil,

along with the increasing popularity of cars, has led to a significant expansion in the asphalt industry. Modern petroleum-derived asphalt has the same strong qualities as natural asphalt, with free of organic impurities and minerals [2].

Most of the asphalt produced today is used for highways. Asphalt paving materials are a sloping black mixture of asphalt cement, sand, and crushed rock. After being heated, hot fumigation is drowned on the road, level trickled, then compressed by a heavy stroller. Asphalt is also used for expansion joints, concrete road, airport runways, tennis courts, playgrounds and floors in buildings. Light forms of petroleum asphalt, called road oils, are sprayed on roads to control dust and connect gravel. Another major use of asphalt is in asphalt shingles and rolled on roofing materials, which usually consists of saturated fibres with asphalt. Additional asphalt applications include tunnels, bridges, dams, reservoirs, stainless steel and rust-resistant metal tubes, automotive sub-sections, and soundproofed walls and ceilings.

## **1.2 Types of Asphalt**

Asphalt is a highly recycled, reused and versatile pavement material. It is used on 94% of the 2.6 million paved roads in America. There are several different types of asphalt pavement, including the following [3]:

1. Porous asphalt: Porous asphalt has existed since the mid-1970s and is mainly used in parking lots to allow water to drain through the road. This road-lining solution is cost-effective and can last more than twenty years.

2. Quiet asphalt: By applying a combination of asphalt or an open layer matrix, this type of pavement with asphalt considerably reduces noise inside and outside residential areas and shops.
3. Thin overlays: Thin overlays improve ride quality and reduce pavement distress, noise levels, and life-cycle costs. It is produced by using warm-mix asphalt and recycled materials.

#### 1.2.1 Hot Mix Asphalt (HMA)

Asphalt hot blending is the most commonly used flex plaster in the United States. It is also known as bitumen, or sometimes just a hot mixture. The (HMA) are mainly classified as thick gradient mix, stone matrix mixes, and open hot mix asphalt. There are also other types of asphalt, but they are limited to maintenance and rehabilitation [4].

##### 1.2.1.1 Hot mix asphalt: Dense mixture

Dense mixture is the most widely used of the hot mix asphalts because it provides excellent sealing properties that allow water to escape from the surface. However, this type of asphalt is ideal for all traffic conditions.

##### 1.2.1.2 Hot mix asphalt: Stone asphalt matrix

The stone asphalt matrix combination has been developed to maximize tenacity and achieve high durability. Because of the manufacturing process, this asphalt mixture is more expensive than ordinary mixed dense mixtures. Its design based on high asphalt content, modified asphalt binder, and fiber. Stone asphalt

matrix has been used since 1980 and can be found in many road and trail applications.

Metal fillers and additives are used to reduce the exhaust gas of the asphalt binder during construction while increasing the amount of asphalt binder used in the mixture and improving the durability of the mixture.

#### 1.2.1.3 Hot mix asphalt: Open-graded mixes

The main difference between open-graded mixes and the two types of asphalt listed above is the permeability characteristic. Open-graded mixes are designed with powder stone and a few grains of sand. There are two classifications for this type of mix, the most popular one is cycle open friction gradient.

#### 1.2.2 Cold mix asphalt (CMA)

Cold asphalt mixing is a combination of mineral aggregates and emulsifying or reducing asphalt with additives. The pool can be made of raw materials or asphalt pavements, also known as asphalt plants. The last option is usually used to save money. Cold mixtures can be produced on-site or at a central location and then transported to the construction site. The flexibility to produce this kind of asphalt outside the construction site is particularly useful for long distance roads [5].

Asphalt cold blends are a kind of asphalt that is usually used as cool mixtures in rural low trafficked streets. Cold mixtures are also used to repair worn road

surfaces and bores when the hot mixture is not readily available and as temporary patches. Additionally, this type of asphalt can be used for the binder, base, top courses and leveling as well as a structural overlay. Cold-mixing materials are durable and flexible, which means that they can heal themselves under the pressure of icy thaw cycles. This makes cold mixtures ideal for non-technical methods.

As with any other form of an overlay, asphalt should only be applied to a pedestal in cold conditions. If any damage occurs to the base or pavement, repairs should be performed before applying the overlay to achieve the best results. The emulsion of the tack coating, particularly in areas with curves or grading, is also recommended.

The life expectancy of cold mix asphalt is around one year. It is very important to use high-quality materials that are properly compacted in order to get the most out of it.

### 1.2.3 Petroleum Asphaltene

Petroleum asphaltene is a specific class of petroleum liquids that is, according to Sheu (2002) [6], not only the most refractory but also generally the heaviest of all oil components. The properties of asphaltene encompass both structure and molecular weight. Nellensteyn believed asphaltenes to be high molecular hydrocarbons that create a colloidal system which becomes adsorbed by surface components. Since that time, numerous researchers have strived to better define the molecular weight, structure, etc., of asphaltene, as they contend

that it is an important base in numerous applications and also improves the production efficiency of petroleum products [7].

#### 1.2.4 Asphalt Cement

Although it can be composed of a variety of substances, asphalt cement is made primarily of bitumen, resins, and absorbed gas. The distillation process for this type of asphalt can be naturally occurring and lead to the formation of asphalt lakes, or it may occur during the petroleum refinement phase. Moreover, the distillation process and type of crude are instrumental in defining both the content and fractional proportions of the various primary and secondary compounds found in asphalt cement [8].

Asphalt cement typically undergoes physical and chemical alterations over the course of time, mainly due to the different reactions of its contents. The most common alteration is stiffening that occurs as the asphalt ages. In order to create different asphalt cement grades, heavy residues are further processed during the refining process. Asphalt cement is currently marketed as “performance grade” (PG) binders and is used according to the traffic load and weather conditions of the intended locations [9].

### **1.3 Performance grade (PG) and Asphalt Binder Pavement**

Performance grade (PG) binders and PBA binders are conceptually similar. The PBA binders are a major building block for the PG System. PBA binders, mostly based on the traditional viscosity testing protocols, introduces the concept

of specifying binders based on the project climatic conditions and binder performances in the pavement. Later, PBA binders adopted some of the fundamental properties (stresses and strains) binder tests developed for PG System. The current PBA binders has evolved to exclusively characterized polymer-modified binder. It is expected that the PBA binders will be replaced by the PG Grades for modified binder (PG Modified) in the near future [10].

#### **1.4 Crude Oil Characterization**

Petroleum crude oils are complex mixtures containing tens of thousands of chemically distinct organic compositions within a dynamic range of 10,000-100,000 in relative abundance [11,12]. The origins of any given crude oil can have a significant impact on the composition. Crude oil widely varies in volatility, density, viscosity, and color and may also contain a solution of inorganic gases, such as nitrogen, carbon dioxide, and hydrogen sulfide. Water is another important component of crude oil. The water has a limited mixing with hydrocarbons, and most of it is found in the form of droplets in an emulsion or free water phase. Usually, water is separated in a good free-face facility, whereas emulsified water removal operations occur in the pre-refining stage.

In oilfield operations, crude oils are generally classified based on the viscosity. Table 1.1. Correlates the viscosity and density of 3 crude oil types to the °API. Light oil or “conventional crude oil” is often produced by primary or secondary recovery process without the addition of heat, chemicals or solvents. These oils have relatively low viscosity and density. Crude oil that is significantly more

viscous and has a lower API gravity (higher density) is called “heavy oil”. These oils are typically produced by enhanced oil recovery techniques and require thermal stimulation or by addition of chemicals. Bitumen or “extra heavy crude oil” are near-solid materials that do not flow freely under ambient conditions. They are extremely viscous and are usually extracted from oil sands mining or through enhanced oil recovery techniques. Overall, the hydrocarbon (as opposed to heteroatom) content of the crude oil may be as high as 97 wt% in the case of light oil or as low as 50 wt% in heavy crude oil and bitumen.

Table 1.1: Classification of Crude Oils

Crude oil type	Viscosity (MPa•s)	Density (kg/m <sup>3</sup> )	°API
light oil	< 100	< 934	> 20
heavy oil	100 to 100,000	934-1000	10 to 20
bitumen	> 100,000	>1000	< 10

Hydrocarbon components in crude oil begin with methane (CH<sub>4</sub>), the simplest of all hydrocarbons. Methane is the most common component in petroleum at high pressure and temperature conditions. Since methane contains one carbon atom, it is often referred to as C1. Similarly, the term C2 is used for ethane (C<sub>2</sub>H<sub>6</sub>), C3 for propane (C<sub>3</sub>H<sub>8</sub>), and so on. In general, the hydrocarbon

components in a crude oil may extend up to C200. Hydrocarbons with seven and more carbon atoms are usually referred to as C7+ fraction or plus fraction.

The C7+ fraction is far more complex than lighter fractions due to the larger number of isomer combinations available to hydrocarbons with increasing carbon number as well as the presence of heteroatoms. A particular C7+ component may belong to one of the following component classes: paraffins, naphthenes, aromatics, resins and asphaltenes.

Paraffins alkanes are straight chain or saturated hydrocarbons, where carbon atoms are linked by single bonds. They can be unbranched (normal- or n-paraffins) or branched (iso- or i-chained).

Naphthenes, also called cycloalkanes, resemble paraffin with one or more cyclic structures. They are carbon atoms linked to ring structures and by single bonds.

Aromatics are components with one or more of the cyclic structures that contain double bonds. Gasoline is the simplest aromatic component. It may be associated with aromatic replacements of the naphthene rings and/or paraffin side chains.

Resins are very aromatic components and their structure is not well-defined. Primarily, they are polar, polynuclear molecules consisting of condensed aromatic rings, aliphatic side chains and few heteroatoms. The asphalt-like resin is bigger and more intense, as well as more polar and aromatic. Figure 1.1 shows the continuum of Saturates, Aromatics, Resins, and Asphaltenes (SARA) In Petroleum.

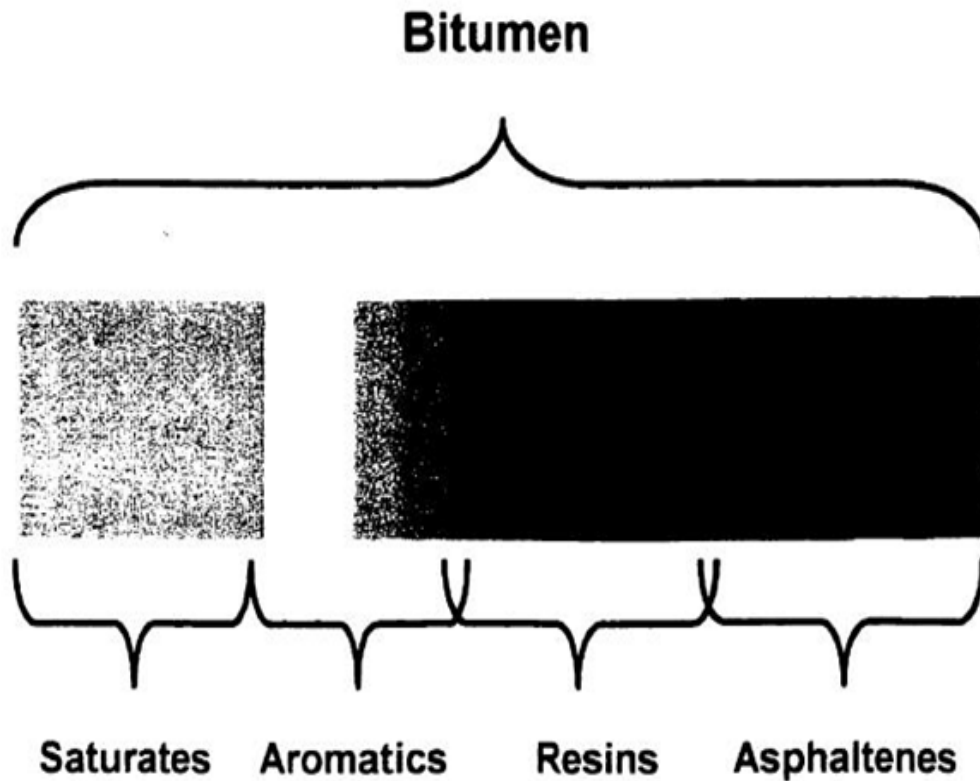


Figure 1.1: Continuum of Saturates, Aromatics, Resins, and Asphaltenes (Sara) In Petroleum [13].

#### 1.4.1 Asphaltenes

The difference between asphaltene and asphalt is that asphaltene refers to any of the dark organic constituents of crude oils and bitumen that are soluble in aromatic solvents but not in aliphatic ones. Furthermore, they are polycyclic aromatic compounds composed of fused benzene rings with aliphatic side chains. Asphaltenes are defined as a soluble class of petroleum, which precipitate from crude oil by adding excessive amounts of solvents such as n-alkane, n-heptane or n-pentane, and are soluble in aromatic solvents such as toluene or benzene.

On the other hand, asphalt is a sticky, black and highly viscous liquid or semi-solid, composed almost entirely of bitumen. It is present in most crude petroleum and in some natural deposits. Asphalt is not a pure element but instead consists of tens of thousands of species that all have similar melting behavior but (usually) different chemical structures, sizes, and shapes.

Asphaltene species can also share some common features, in that they are polynuclear aromatics which contain n-alkane chains, cyclic alkanes, and heterogeneous atoms such as sulfur, nitrogen, oxygen, nickel, vanadium, and iron. (Moschopedis et al., 1976) created a list of asphaltenes extracted from various crude oils worldwide (see Table 1.2). The hydrogen-to-carbon (H / C) atomic ratios of C5- asphalt were found to be  $1.2 \pm 0.5\%$  [11]. A typical asphaltene sulfur molecule may contain Thiophanes, thiols, sulfides, disulfides and forms of oxidation. Nitrogen can also be found as pyrroles and pyridines structures. Oxygen has been identified in carboxylic, phenolic and ketonic locations, and metals (nickel and vanadium) are present as porphyrins.

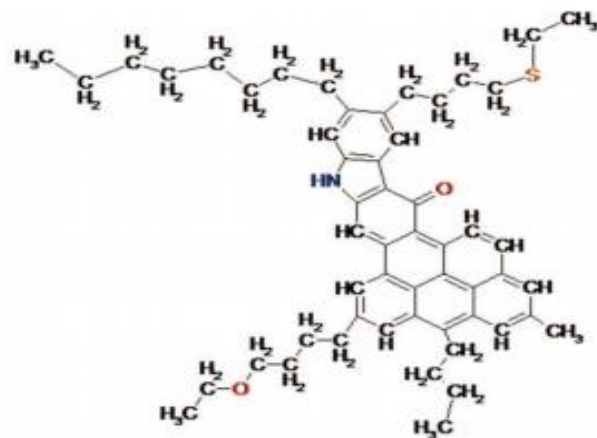
Asphaltenes are generally claimed to be the “highly polar” fraction in the crude oil. This is based on the fact that asphalt is insoluble in n-heptane, non-polar solvents. However, asphalt is easily soluble in solvents that are relatively non-polar, such as benzene, toluene, and dichloromethane, as well as in polar solvents such as water, glycerine and methanol. Thus, asphalt can be non-polar and chemically polar compared with other components of crude oil.

Table 1.2: Elemental Composition of Various Asphaltenes

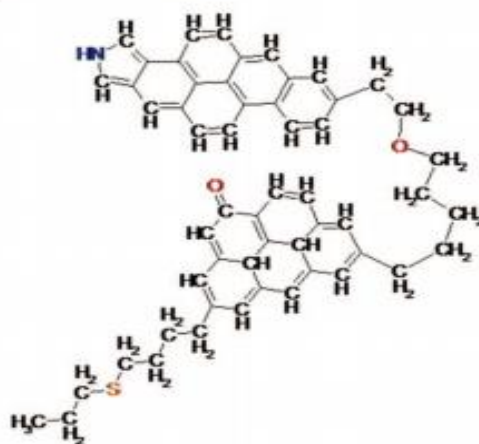
Source	Composition (wt %)					Atomic Ratios			
	C	H	N	O	S	H/C	N/C	O/C	S/C
Canada	79.0	8.0	1.0	3.9	8.1	1.21	0.011	0.037	0.038
Iran	83.7	7.8	1.7	1.0	5.8	1.19	0.017	0.009	0.026
Iraq	80.6	7.7	0.8	0.3	9.7	1.15	0.009	0.003	0.045
Kuwait	82.2	8.0	1.7	0.6	7.6	1.17	0.017	0.005	0.035
Mexico	81.4	8.0	0.6	1.7	8.3	1.18	0.006	0.016	0.038
Sicily	81.7	8.8	1.5	1.8	6.3	1.29	0.016	0.017	0.029
USA	84.5	7.4	0.8	1.7	5.6	1.05	0.008	0.015	0.025
Venezuela	84.2	7.9	2.0	1.6	4.5	1.13	0.020	0.014	0.020

#### 1.4.2 Molecular Structure

There is an ongoing debate regarding the molecular composition of asphalt, especially in reference to the size of the aromatic groups and how they are linked to other structural groups. A molecular model of an asphaltene molecule is provided below as (continental) structures and dispersed (Archipelago) structures, as shown in Figure 1.2.



(a) Continental



(b) Archipelago

Figure 1.2: Model of asphaltene molecules: a) the “continental” type, and b) the “archipelago” type [14]

The intensive structure of the molecule represents a typical asphaltene, as the nucleus of aromatic contains a large number of fused rings (it usually consists of more than seven rings) with aliphatic groups. A condensed structure interpretation is supported by data obtained from proton (<sup>1</sup>H nuclear) magnetic resonance spectroscopy, X-ray diffraction, and fluorescence polarization experiments [15]. It represents the structure of a typically scattered asphaltene molecule as a collection of small aromatic groups linked by bridges. This interpretation is based on the

structure of dispersant on data from pyrolysis, oxidation, and thermal degradation and small-angle neutron scattering techniques [16]. High-resolution mass spectrometry data show that both structures may actually exist in the oil [17].

#### 1.4.3 Density

Gravimetric measurements are typically used to obtain the density of asphalt. Solid asphalt from crude oil density is reported to be between 1170 and 1280 kg/m<sup>3</sup> [18]. The density of asphalt with a smaller H / C ratio (more aromatic) is greater than asphalt with a larger proportion of H / C. The effective liquid density of asphaltene in mixtures was measured using an indirect method [19]. The density range reported by this method of 1100-1200 kg/m<sup>3</sup> of asphalt came from a variety of sources.

#### 1.4.4 Surface Activity

Several studies on the characterization of surface active material have focused on oil and water interface, including asphaltenes. Asphalt surface activity can be attributed to the functional water groups, which are an integral part of the structure of hydrophobic hydrocarbons. For example, acidic and basic heteroatom groups containing oxygen, nitrogen and sulphur are hydrophilic. Hence, asphaltenes behave as surfactants and can adsorb at the water-oil interface. The adsorbed asphaltenes contribute to the formation of stable emulsions that make oil-water separation difficult and thereby causing problems in downstream operations [20].

The most frequently cited evidence for interface activity of asphaltene is based on measurements of interfacial tension. There is a general reduction in the concentration of asphalt surface tension between the oil sample (for example, mixtures of heptane-toluene) and water [21]. Surface tension in the media can result from substances that are very acidic or basic, suggesting that both acidic and basic groups interact in the interface [22].

Resins are also considered as one of the active surfaces of crude oil components. For example, the creation of films and interfaces of most stable emulsions occurs through a combination of asphalt and resins [23]. However, according to Gafonova and Yarranton (2001) [24], resins tend to destabilize the emulsions model. Using the thin liquid film-pressure balance apparatus, Taylor et al. (2002) [25] observed that toluene-asphaltene films and toluene-bitumen can be compressed to the same thickness (8.5 nm bilayer), so it was concluded that the surface-active substances were at the front of asphalt bitumen water in the first place. In addition, it was noted that upon removal of high molar mass asphaltenes, the bilayer decreased from 8.5 nm to 5.1 to 7.3 nm, the film stability will be reduced.

The surface chemistry of the elements active in the oil-water interface has been examined as well. Shaw and others (1999) [26] claimed that the active surface or interface material components of bitumen in water systems are polar compounds and contain oxygen. Wu (2003) [27] developed an experimental methodology for isolating interface material from Athabasca bitumen emulsion heavy water. He pointed out the elements that interface material analysis contained H / C atomic

ratio of 1.13 above the onset of the rains, while the material interfaces isolated below the start of precipitation consisting of salts of carboxylic with a ratio H / C 1.32. A high-resolution mass spectrum analysis shows that the interface material is comprised of very intense aromatics in layered structures of O<sub>2</sub>, O<sub>2</sub>S and O<sub>3</sub>S, as well as acidic and basic N- and NS-class homogeneous structures [28].

### **1.5 Asphalt Physical Properties**

Asphalt can be classified by chemical composition and physical properties. The road-lining industry usually relies on the physical characteristics of performance marking, although the physical properties of asphalt are a direct result of their chemical composition. The most important physical properties are as follows: [29]

- **Durability.** Durability is a measure of how the physical properties of asphalt are altered with age (sometimes referred to as curing). In general, the viscosity increases as an asphalt binder becomes stronger and more brittle.
- **Study of flow properties.** Rheology is the study of deformation and flow of matter. The deformation and flow of asphalt binder are important in pavement performance. If they are deformed and flowing, they can be too susceptible to vandalism and bleed, while those that are severely severe may be prone to fatigue cracking. Rama is closely related to deformation as biologically documented asphalt. The rheological properties of asphalt binder vary with temperature, so the rheological characterization involves two main considerations. First, for a complete description of the asphalt binder, its rheological properties must be

studied over the temperatures that may be encountered during their lifetime. Second, to compare the different asphalt folders, their properties must be measured at some common reference temperature.

- **Safety.** Asphalt cement, like most other materials, lets off steam when heated. At very high temperatures (much higher than those experienced in the manufacture and construction of (HMA), asphalt cement can release enough steam to increase the volatile concentration directly above the asphalt cement to the point where it will be ignited (flash) when exposed to a spark or open flame. This is called the flash point. For safety reasons, the flash point of asphalt cement is tested and controlled.

- **Purity.** Asphalt cement must contain mostly unpolluted bitumen, as impurities can be harmful to asphalt performance.

### **1.6 X-ray Diffraction (XRD)**

X-ray diffraction depends on the ability of the double wave/particle X-ray to obtain information on the structure of crystalline materials. The primary use of technology is to identify and characterize compounds based on their diffraction patterns [30].

The predominant effect that occurs after an incident beam cooperates with a monochromatic X-ray with an aim material is the scattering of those X-rays from the atoms within the target material. In materials with a uniform structure (i.e., crystalline), dispersed X-rays are exposed to constructive and destructive interventions. This is known as the process of diffraction. X-ray diffraction crystals are described by the Bragg law ( $n\lambda = 2d \sin \theta$ ) this law refers to the

wavelength ( $\lambda$ ) of the electromagnetic radiation ( $n$ ) of the diffraction angle  $\theta$  and d-spacing in a crystalline sample., which gives information on the structure, size and shape of a unit cell of material. The intensity or strength of the diffracted X-rays depends on the type and arrangement of the atoms in the crystalline structure.

However, while most materials are not considered single crystals, there are some crystals that are small in size and moving in all possible directions. These are called polycrystalline compounds or powder. If a powder sample with polycrystalline character is randomly arranged in the X-ray beam, the beam will understand all possible inter-atomic planes. Moreover, when the experimental angle is systematically changed, all diffraction peaks are detected by the powder.

The (Bragg-Brittano) diffractometer is the most widely used technique for diffraction tools. This geometry offers the advantages of a high-precision beam intensity analysis at the expense of very accurate alignment requirements and carefully prepared samples. In addition, it requires that the distance between the source and the sample be constant and equal to the sample distance to the detector. Alignment errors often have difficulties in determining the level and determination of the wrong quantities. A wrong sample can lead to unacceptable errors in the offset test. Restrictions on the flattening, roughness, and positioning of samples are excluded in the test sample line. In addition, they often use traditional zebra systems on large devices with high energy requirements, as well as energy X-ray sources of high X-ray of the flow of the sample, which increases the yaw of the detected scanning signals. These sources can have large excitation

zones which are often unfavorable for analyzing small sample diffractions or characteristics.

With multi-faceted X-ray optics, many of these defects and limitations can be overcome to promote zebrafish applications. Thus, the multi-ring parallel focus becomes a semi-parallel housing with a small distance and can be used as a parallel beam shears engineering tool, which greatly reduces and eliminates many sources of error in the top position. Here, the technique of baravoxing intensity can be used by applying the factors of shape, roughness, flatness and transparency position. The United Optics Center connects X-ray sources and spaced alignments, and focus on a small packet on the surface of the sample small diameter, such as ten-micrometer applications. Both types of optics (polycyclic and direct X-ray) have the very high intensity to the sample surface, so zebrafish systems can be used as energy sources for low X-rays in order to reduce the size of the instrument as well as the cost and performance requirements [31].

X-ray diffraction using X-ray optics has been applied to many different types of applications, including thin-film analysis, tissue texture assessment, crystalline phase monitoring and structure, and sample strain and strain investigation.

### **1.7 Bragg's Diffraction**

When the X-ray hits the crystal, the electromagnetic waves (EM) enter the crystal structure. Each plane of atoms in the crystal reflects part of the waves. The reflected waves of different planes overlap with each other and lead to a so-called

reflection beam, which is at a well-defined angle of  $2\theta$  to the incident beam, as shown in Fig. 1.3. The beam of the incident is diffracted by the crystal structure. As can be observed, a portion of the incident beam passes through the crystal and part of the dispersion beam. Furthermore, the diffracted beams exist only in certain directions. These diffraction trends correspond to well-defined diffraction angles of  $2\theta$  as shown in Figure 1.3. The diffraction angle,  $2\theta$ , the X-ray wavelength, and the distance between satellites  $d$  are known for the diffraction planes within the crystal by the diffraction condition of the Bragg's law equation,  $2d \sin \theta = n\lambda$ .

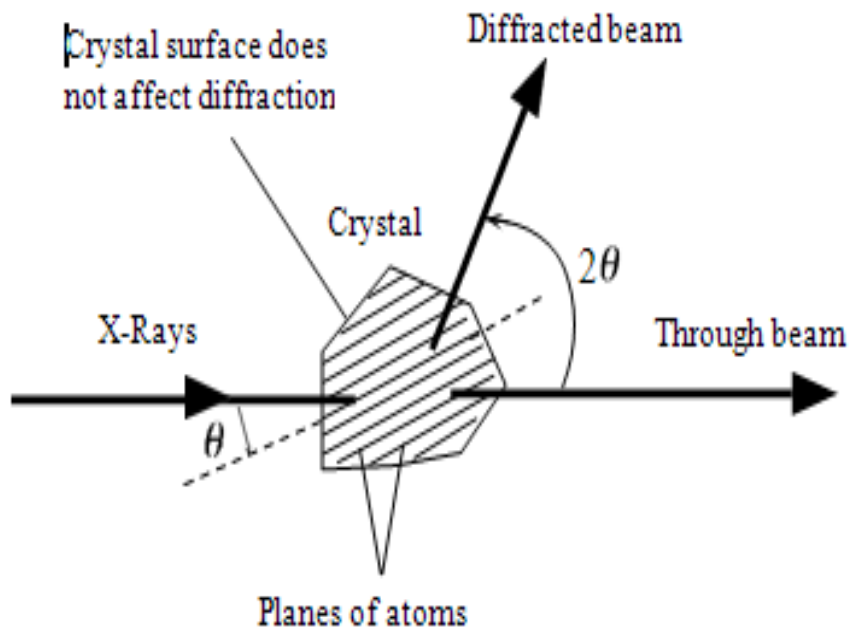


Figure 1.3: A schematic illustration of x-ray diffraction by a crystal [32].

When the X-ray beam is on a crystal, a part of it passes while a part of it is scattered by a  $2\theta$ , depending on the wavelength of the X-ray beam and the atomic atoms in the crystal causing the diffraction. The surface of the crystal, regardless

of its shape, does not affect the diffraction process, since X-rays penetrate the crystal and are then dispersed through a series of atomic planes [32].

### **1.8 Objectives of the Research**

The objective of this research is to investigate XRD analysis on asphalt structure, properties and performance. Furthermore, this work is intended to develop a main pavement deterioration model for asphalt pavements, focusing on the molecular level of asphalt binders. A total of 5 different samples of asphalt binders are taken from different parts of Canada and tested in the laboratory for aging and investigating the composition of the aggregates at a microscopic level. The aging of asphalt specimens is simulated using three of the major mathematical functions (pseudo-Voigt, Pearson VII, and generalized Fermi function), representing a simulation based on real aging of asphalts from the specimens. The XRD data will show that it is possible to differentiate asphalts of different standards and classifications through peak centroid and other parameters (e.g., aromaticity and crystallite size).

## Chapter 2

### Literature Review

Asphalt binders are most commonly characterized by their physical properties. An asphalt binder's physical properties directly describe how it will perform as a constituent in asphalt concrete (AC). Although asphalt binder tests and specifications are developed to more accurately characterize asphalt binders for use in (AC) pavements, these are specifically designed to understand asphalt binders performance parameters, such as rutting, fatigue cracking, and thermal cracking.

### 2.1 Internal Structure of Asphalt

Masad, Muhunthan, Shashidhar, and Harman developed computerized procedures for the integrated analysis of digital images to determine the internal structure of AC. This has been described in terms of the internal structure of the overall trend, aggregate gradation, and inter-earned leisure air distribution. They found a tendency to prefer the direction of the overall structure of the increase with the pressure until a certain pressure was exerted. After that, the overall structure was turned more at random. The vacuum distribution in the samples was found to be non-uniform, so the focus was more on internal voids in the upper and lower parts of the sample wrap pressure. Spaces in percentage measurements using an image from computed tomography X-ray images analysis compared well with voids percentages measured in the laboratory [33].

A comparison between the internal structures of the gyratory specimens with the field cores showed that the gyratory specimens reached the initial aggregate orientation of the field cores at a higher number of gyrations, whereas they reached the percentage air voids in cores at a lower number of gyrations. The coarse aggregate gradation of gyratory compacted specimens was well captured using image analysis techniques. There was no change in gradation with compaction. The new procedure's characterization and image analysis will affect many areas of the asphalt binder studies, as these new measures are useful tools to describe and compare the asphalt binder materials produced using various laboratory equipment, mix designs. In addition, the procedures improve the mechanical models by providing specific parameters of internal structure to be included in the constituent relations. In this study, attention was limited to examining the internal structure of the samples prepared in the laboratory and cores recovered from the field. The same techniques, however, will be useful for the study of the characteristics of interior materials according to the pressure they are under in the field.

In the past, Caltrans has classified binders using viscosity grading based on the aged residue (AR) system. More recently, Caltrans used the performance graded (PG) system. For polymer modified binder, Caltrans has also used the performance-based binder(PBA) system [34].

## 2.2 Self-Association and Molar Mass

The molar mass of asphaltene has been a controversial issue for many years. Two of the main causes of the controversy are the polydisperse nature of the asphaltene and the association behavior of asphaltenes even at low concentrations. As a result, any experimental technique for measuring the molar mass is uncertain. The development of advanced mass spectrometry techniques in recent years has helped to reach a consensus on asphaltene molecule (or monomer) molar mass. Mullins (2010) summarized some experimental techniques (classified as mass spectrometry and molecular diffusion methods) to report the molar mass of asphaltene, using monomers in the range from 400-1000 g / mol [35].

Since the asphaltene can be associated with each other even in dilute solutions, a number of studies have been conducted to investigate the behavior of self-association. Self-association has been experimentally observed from the trends of asphaltene apparent molar mass with concentration. The apparent molar mass is the product of the monomer molar mass and the aggregation number of the self-associated asphaltenes. Some of the experimental methods used to observe the asphaltene self-association are vapor pressure osmometry, interfacial tension measurements from a drop volume tensiometer (Yarranton et al., 2000) [36], small-angle X-ray and neutron scattering measurements (Shaw et al., 1995; Spiecker et al., 2003) [37,38]. Differential scanning calorimetry (Anderson & Birdi, 1991) [39] dielectric spectroscopy (a two-step laser mass spectrometry) and Fourier transform ion cyclotron resonance mass spectrometer [40].

Vapour pressure osmometry provides what is probably the most direct measure of asphaltene association. For example, the apparent molar mass of asphaltenes in toluene increases from approximately 1000 to 5000+ g/mol as the concentration of asphaltenes increases from 2 to 40 g/L. In most cases, at concentrations above 10 g/L, the apparent molar mass approaches a constant value in the order of 5000 to 10,000 g/mol. Hence, self-associated asphaltenes consist of three to ten molecules per aggregate on an average. Also, the extent of asphaltene self-association has been found to decrease in better solvents (such as toluene), at higher temperatures and with increasing resin content [41].

The relative significance of the forces holding the aggregates together is unknown. A molecular mechanics investigation of asphaltene aggregation has emphasized the importance of hydrogen bonding [42]. Hydrogen bonding among asphaltene molecules is likely due to heteroatoms in functional groups. However, since asphaltenes consist mainly of carbon and hydrogen atoms, it is also important to consider van der Waals interaction forces. Although van der Waals forces are very weak, its overall contribution could be significant once the asphaltene molecules are highly packed [43].

### **2.3 SAXS and SANS**

Herzog et al. (1988) achieved small-angle x-ray scattering (SAXS) experiments using a synchrotron x-ray source for some asphaltene dispersions in organic solvents as well as natural solvents (maltenes). They interpreted asphaltene species as thin, large and porous particles with varying radius and a lateral

extension possibly greater than 80nm [44]. This interpretation has been supported by several other experimental observations including those by Xu et al. (1995) [45], who used SAXS to demonstrate the existence of particles with sizes ranging from 3 to 15nm in crude oils diluted in aromatic solvents. Small angle neutron scattering (SANS), used by Ravey et al. (1988) [46], revealed particle sizes in this same size range. Also, they concluded that the physical dimensions and shape of the asphaltene aggregates was a function of solvent and temperature of investigation. XRD was used by Siddiqui et al., (2002) [47] to investigate the structure characterization and the aging pattern of asphalt binders. Asphaltene has high resistance to cracking. As a result, it is difficult to biodegradable, due to presence of heavy metal components. On the other hand, the presence of high percentage of asphaltene has an advantage in obtaining quality pavements in hot and cold locations.

#### **2.4 X-ray Spectral Line Shape Analysis of Asphalt Binders**

A comparison was made by Siddiqui et al., [47] between XRD pattern fit by Pearson VII and pseudo-Voigt directly on the generalized Fermi function modeling and measurement of aromatic crystalline parameters. They can be explained by the mixed results of the data function for Generalized Fermi Function to the Pearson VII function results and the results in the pseudo-Voigt functions peak and installation profile, which were not similar to the XRD data format.

A total of 17 samples were obtained from the two assays of different sites at a low temperature and at one week of age. The analysis of the results suggests that the aging process can affect the X-ray data due to changes in chemical (oxidation), aromatic calculation and crystalline parameters. The results showed a correlation between Pearson VII, pseudo-Voigt and GFF crystal size in some of the parameters ( $d_\gamma$ ,  $L_a$ ,  $L_c$ ,  $M$ ) more than others ( $f_a$ ,  $d_m$ ), as well as in some of the properties of experiments on the XRD asphalt binders. Figure 2.1 illustrates a cross section of asphaltene cluster structure model, whereas,  $L_a$  is the aromatic sheet diameter,  $L_c$  approximate height of aromatic sheet stack,  $d_m$  presents distance of inter-aromatic layer,  $d_\gamma$  presents distance of inter-chain and  $M$  approximate number of related aromatic sheets in the stacked cluster. The molecules-associated asphaltene groups with aromatic plates stacked relatively stable up to 150°C, and the distance between the aromatic platelets ( $d_m$ ) and the number of aromatic leaves in the cluster of one group ( $M$ ) was uniform in these asphaltene species.

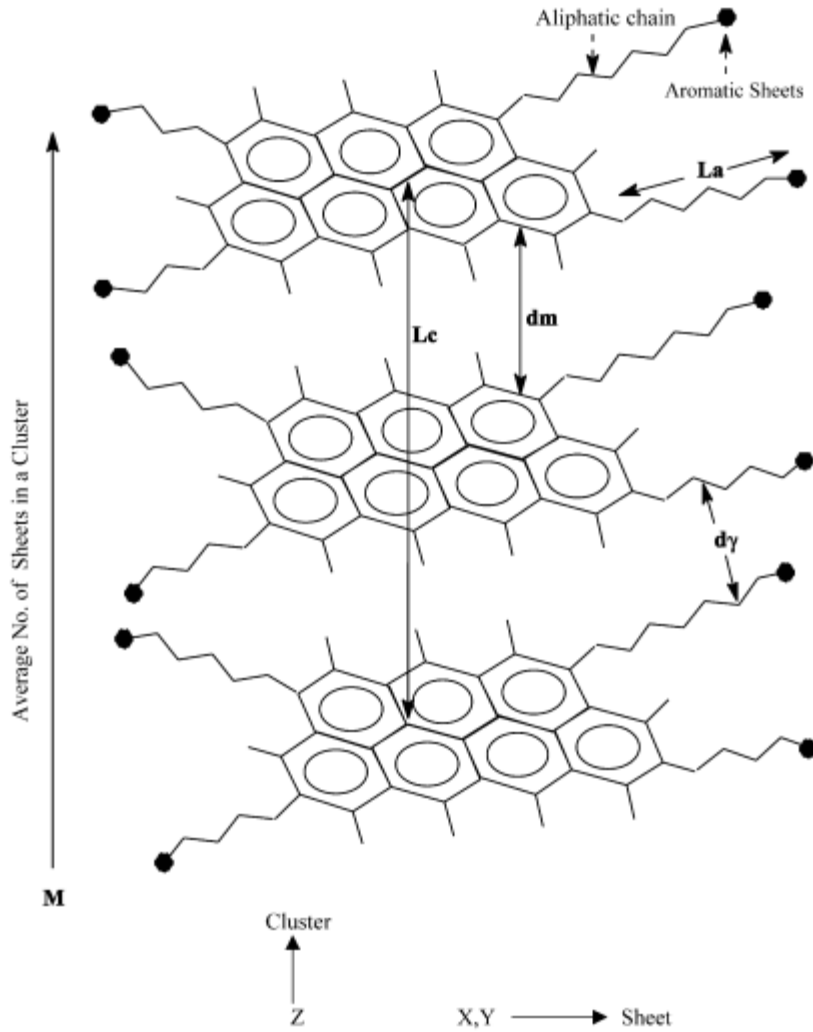


Figure 2.1: The cross section of asphaltene cluster structure model [47]

Further analysis of results obtained in this research shows that XRD provides insight into the structural properties of asphalt and synthetic binders, which is important for understanding the aging process of asphalt folders and asphalt pavement cement. Since the results for the XRD binder asphalt in the previous civil engineering tests were completed. Hence, it is reasonable to expect in the future that the asphalt binder XRD results play a role in the prediction of the

performance and durability of asphalt in the roadway, and asphalt binder conversion into fuel lighter [48].

## **2.5 Aging of Asphalt Binder**

The aging of asphalt materials in the field as well as during the accelerated aging in the laboratory is a very complex process. It is generally agreed that the aging process is carried out in two separate steps: (1) during construction (mixing, placing and printing); and (2) during the shelf life of the plaster. This aging generally results in a change in the molecular size distribution of the asphalt binder. In particular, an increase in the molecular size leads to an increase in the viscosity of the asphalt binder, whereas in the field, this leads to fragility and failure [49,50].

The asphalt aging is one of the main factors that are responsible for the deterioration of pavement of asphalt in the roads, and it decreases under heavy traffic conditions. The aging method of asphalt binder has been studied extensively by [51]. The majority of the procedure involves a temperature of about 100°C to 200°C. It found by the author that the correlation of the laboratory method relative to the aging field was almost created on the basis of the number of factors that are limited to left without consideration and this includes penetration, softening, etc. It was observed and analyzed from the research that the use of (XRD and GFF analysis) the effects of the aging of asphalt binder caused by improper mix and weather changes in the petroleum asphalts of the Canadians that have been used to construct all of the transportation road networks.

## 2.6 XRD

Since the mid-1900s, X-ray diffraction has been developed to the point that it can now be used across a broad spectrum of research fields. For instance, Ergun and Tiensuu (1959) [52] applied XRD to investigate the structure of coal. The researchers found the method useful for measuring the distance between aromatic layers in relation to the grapheme (002) band that manifests at around  $26^\circ$ , as well as for measuring the distance between aliphatic layers that manifests at around  $20^\circ$ . Moreover, XRD has been found to offer important details about asphaltene's internal structure, including for the extraction of molecular crystallite parameters in relation to aggregates [53].

Because asphaltene aromatic cores can be arranged to create a stack of aromatic sheets, we can use XRD analysis, as stacking enables the formation of crystallites. Siddiqui et al. (2002) stated that XRD can also be used to analyze additional crystallite parameters like polar aromatics, naphthene aromatics, and saturate fractions; they applied the approach to Arabian asphalts [47]. The atoms of a crystalline material are arranged in a regular repetitive pattern, which includes high-order crystals and three-dimensional structures. When an X-ray beam hits such a structure, electrons vibrate along the path at the same frequency as the incident X-ray. These vibrating electrons absorb a part of the X-ray energy and serve as a source for new wave fronts. Energy is then emitted as X-radiation from the same frequency and wavelength absorbed. The waves normally overlap with one another and no detection packet is emitted. However, if the wavelength, frequency, and structure of the crystal and angle of the action are correct, those

involved in this stage will wave and mutually reinforce each other, leading to a beam that can be detected [54].

Figure 2.2 shows the mean profiles obtained from CAP 50/70 produced by the Repar and Replan Refineries. The profiles were obtained in 0, 60, 120, 180, 210, 330, 390 and 430 days. Each profile, for each date, is an average profile from ten profiles (n=10) [50].

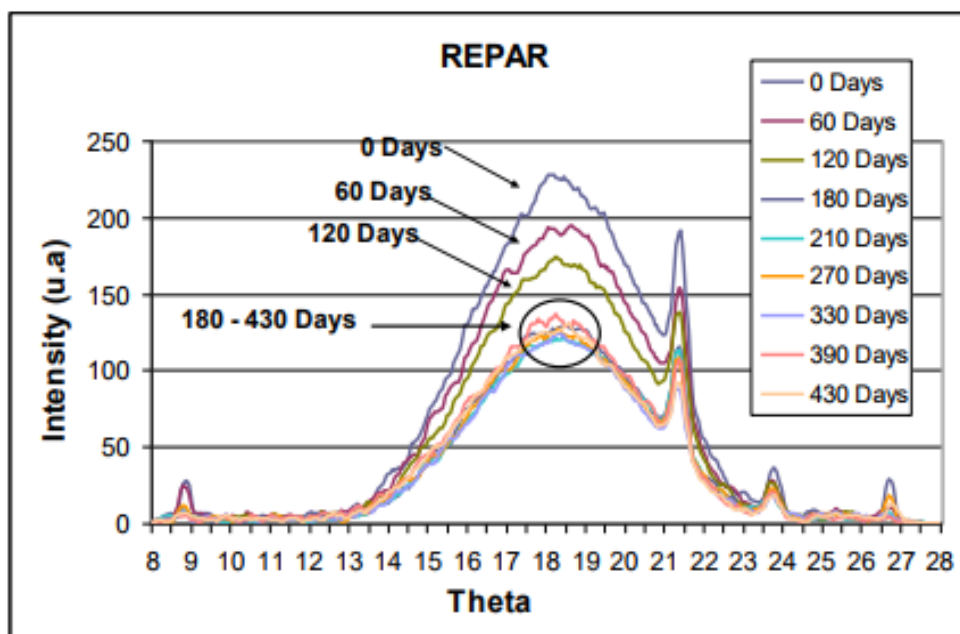


Figure 2.2: Means profiles from cap 50/70 by Repar refinery in each time [55].

The structural studies of asphaltenes crude oil were carried out from the X-ray diffraction. XRD was performed with copper K- $\alpha$  radiation works at 40 kV and 40 mA, with 0.001degrees  $2\theta$  sampling rate per second. XRD data processing was used for the first time with the characteristics of the Pearson VII,

subsequently with pseudo-Voigt features, and then in Mathematica © modeling of the generalized Fermi function (GFF). These also contain several different backgrounds (linear, exponential, and Lorentzian). The results are discussed based on their accuracy with different sets of background and line profiles [56].

## 2.7 Modeling Asphalt as a Cubic Material (Yen Model)

XRD Asphaltene has four peaks. The first peak gamma is the packing distance of saturated structures derived from X-rays diffused by aliphatic chains or saturated rings. The peak of graphene (002) is derived from the X-ray diffraction by aromatic particle stacks. The peak (10) and (11) in the X-ray diffraction are from the air cell of the aromatics (see Fig. 2.3). This corresponds to the first and second neighbors closest to the ring compounds [57].

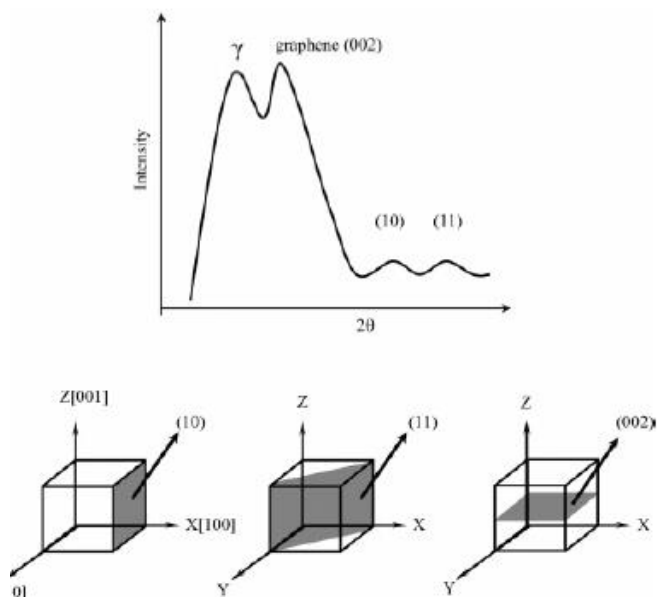


Figure 2.3: X-ray diffraction pattern peaks and corresponding planes [57]

In general, sharp XRD pattern peaks have highly crystalline samples with a high degree of remote control. In the case of asphalt, solid crystals have a good long-term yield in some directions, while in others only in a short-range order. This is the obvious reason why there are sharp peaks in all diffraction patterns.

## **2.8 Modified Yen model (the Yen-Mullins model)**

In recent years, there has been renewed research interest around asphaltene properties, with a focus on molecular weight and structure. Mullins (2010) discussed how long-standing disputes over asphaltene's molecular weight are beginning to be resolved through the application of various accepted techniques. Despite these promising changes, asphaltene properties remain for all intents and purposes still lacking in a clear definition due mainly to the complexity of the material's structure. Figure 2.4 provides some details about its properties.

In exploring the many facets of asphaltene, we can use the modified Yen model (the Yen-Mullins model) to deal with the enormous amount of data [35]. The modified Yen model represents a first principle approach and can thus be applied towards asphaltene properties in bulk as a way to break down the analysis into more manageable portions.

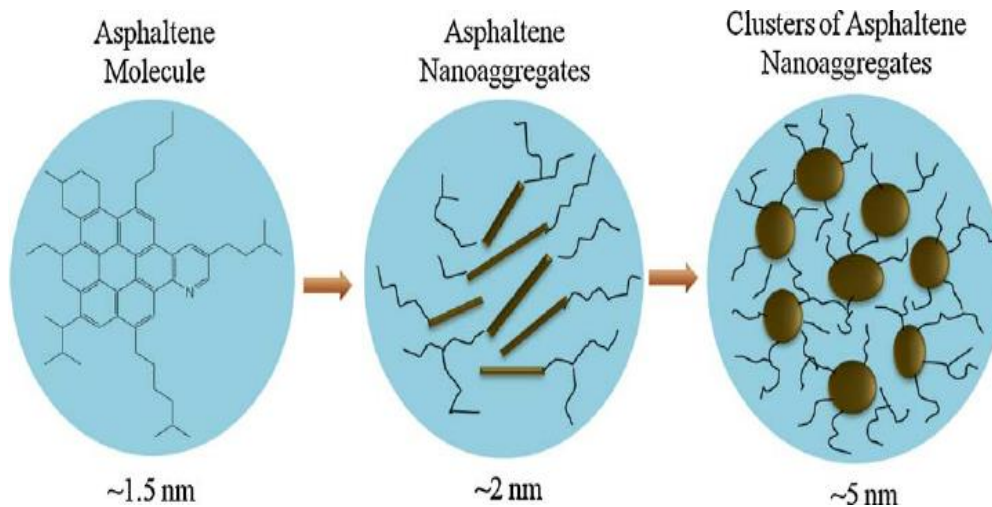


Figure 2.4: The Yen–Mullins Model [58]

Mullins and colleagues had further investigated asphaltene, discovering that the asphaltene nanoscience model can be correlated to the modified Yen model. This is an exciting discovery, as it may prove to resolve, on the nano-scale, many contentious issues regarding the behavior of compounds, including composition and structure [58].

## 2.9 Asphalt Chemical Components and Modification Efforts

Most asphalt particles mainly composed of carbon and hydrogen contain one or more elements of sulfur, nitrogen and/or oxygen. The reaction of heterodoxies and hydrocarbons leads to the unique chemical and physical properties of various asphalt mixtures [59,60].

Research carried out in the Netherlands has shown that nano coat modifications improve some properties of asphalt mats and asphalt mixtures, but further research is needed before they can be applied extensively [61].

In China, similar studies were carried out on calcium carbonate-nano (nano- $\text{CaCO}_3$ )-modified asphalt [62]. It was discovered that the nano- $\text{CaCO}_3$  can improve the asphalt resistance as well as improve the low-temperature hardness. The mixture of nano- $\text{CaCO}_3$  and asphalt has been shown to form a uniform and constant system which improves the asphalt temperature at high temperatures. However, the mechanism of the behavior of asphalt materials with this modification is not well understood.

Also in China, the (montmorillonite) has been modified by the properties of styrene-butadiene-styrene (SBS) modified asphaltic polymers by dissolving the mixture with various contents of sodium montmorillonite (Na-MMT) and organic montmorillonite (OMMT) [63]. It was found that the addition of Na-MMT and OMMT increases the modified asphalt viscosity of the asphalt. Therefore, compared to the original asphalt or modified asphalt SBS, MMT-modified asphalt may form an intercalated structure. OMMT modified asphalt proved to be an impregnated structure, while asphalt and octoxide can form a laminated structure [64].

## **2.10 Low Temperature and Fatigue Cracking in Asphalt Pavement**

Low-temperature cracking, also known as heat cracking or cold cracking, is one of the main limitations observed on asphalt pavements, especially in North America, due to unusually large temperature drops that can occur at regular intervals in the cold winter months. However, this type of distress is also observed

in other parts of the world where the temperature not often falls below freezing, such as in desert climates due to large, absolute, daily temperature fluctuations.

This form of pavement distress has been recognized as a commonly existing problem which is induced by the effects of temperature and the quality of the asphalt pavement. Fatigue cracking is closely associated with repeated traffic loads flexing the asphalt pavement layer which is capable of causing jagged cracks that eventually interconnect to form a pattern often referred to as “alligator cracking”., as shown in Figure 2.5 [65].



Figure 2.5: Alligator-type fatigue cracks typically due to load (traffic) distress [66].



Figure 2.6: Longitudinal and transverse cracks typically due to thermal effects [67].

In the last two decades, important research has shown that the mechanism of these types of road failure (that is thermal cracking) occurs when "internal stress is built up and the deflation-induced low-temperature strength exceeds or the cooling rate rises significantly" [68]. Essentially, as the temperature drops, this leads to stress growth and consequently results in stress relaxation which ultimately causes a microcrack (small crack) to develop at the edge of the surface of the pavement. Figure 2.6 illustrates fatigue cracks typically due to load (traffic) distress. More importantly, repeated thermal stress and repeated loading effect can have a significant impact on the asphalt pavement, as the entire asphalt mix has been weakened by traffic loads, potentially resulting in road failure [69].

## **2.11 Morphological Characterization**

The morphology was characterized as modified nanoclay asphalt, using X-ray diffraction techniques (XRD). XRD was utilized to provide a quantitative analysis of the distance of exhibition buildings and to provide a means for determining the extent of the dispersion of nanoclay in a binder. The XRD was individually performed on the original binder and nanoclay a prior to the modified nanoclay binder also being tested. The first provided a useful guide for the interpretation of combined XRD peaks arising from the modified binder test. These tests were performed only on a nanoclay modulation because the impulse was to verify the efficiency of the nanoclay dispersion rate initiated by the mixing process. A higher dispersion rate is required, as nanoclays tend to bond because of their inherent electrostatic charge.

XRD points out that nanosize particles are uniformly dispersed in the asphalt matrix. This confirms that the mixing technique used is effective to create the peeling of nano-particles within the asphalt matrix [70].

## Chapter 3

### Methodology

#### 3.1 Instrument and measuring principle

The XRD diffraction pattern analysis is based on the constructive interference of monochromatic X-rays from crystalline samples: an X-ray is generated by a cathode ray tube, filtered to produce monochromatic radiation, and then directed to the sample. The interaction between the incident beams and the specimen leads to beam deflection when the Bragg's law is satisfied ( $n\lambda = 2d \sin \theta$ ). This law refers to the wavelength of the electromagnetic radiation of the diffraction angle and d-spacing in a crystalline sample.

The characteristic X-ray diffraction pattern produced by typical XRD analysis provides a unique "fingerprint" of the crystals in the sample. Given a corresponding interpretation in comparison to standard reference patterns and measurements, this footprint makes it possible to determine a crystalline form.

#### 3.2 Demonstration of X-ray diffraction

The objective here is to observe one method of evaluating atomic crystalline structure by using X-ray diffraction to understand the use of Bragg's law and its relation to the crystal structure. X-ray diffraction can be used to determine the crystal structure of lattice materials and laboratories. This information can then be used to determine the material for analysis since every element in the periodic

table has a unique combination of capillary structure and is labeled at room temperature.

When an X-ray is directed at a crystal, the beam hits the atoms and produces two types of X-rays: white X-rays and X-rays. White X-rays comprise a wide range of wavelengths and are irrelevant in this experiment. Line X-rays occur when an electron is released from an inner shell of an atom. Bragg's law is used to determine the crystal parameters of the characteristic interference pattern. X-rays that strike the crystal have a wavelength almost equal to the distance between the atoms in the crystal lattice.

Bragg's law can be visualized by looking at a cubic crystal lattice consisting of parallel planes of atoms. This occurs when the incident beam reaches the parallel planes at certain angles, known as the Bragg angles. In the case of non-reflection, the waves leave the crystal from the phase and mutually cancel each other out. Figure 3.1 shows the reflection of X-rays in the (Miller indices  $hkl$ ) reflected planes of the crystal [71].

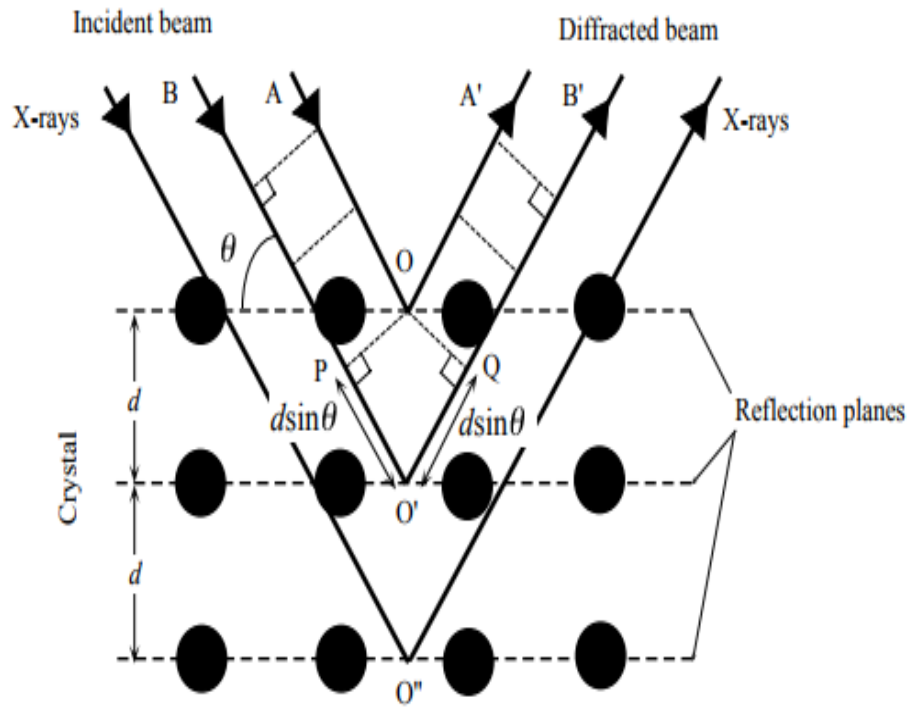


Figure 3.1: Reflection of X-rays in the (hkl) planes of a crystal [32]

In order to understand the origin of the diffraction and the presence of certain angles of refraction, the X-ray beam will penetrate the crystal structure and be reflected by a certain number of atomic planes (see Figure 3.1). We can consider the X-ray beam as many parallel waves in phase.

The diffraction includes the waves reflected by the different atomic planes in the crystal. For the sake of simplicity, let us consider two waves, A and B (in X-ray), reflected by two successive atomic planes in the crystal. Wave A is reflected first from plane 1, while wave B is shown from plane 2, as illustrated in Fig. 3.1.

Note that the  $\theta$  is not the angle between the incident beam and the sample surface, but the angle between the incident beam and the crystallographic plane that generates diffraction. Diffractometers can have various types of geometric arrangements to enable collection of X-ray data. The majority of commercially available diffractometers use the Bragg–Brentano arrangement, in which the X-ray incident beam is fixed, but a sample stage rotates around the axis perpendicular to the figure plane of Figure 3.2 in order to change the incident angle. The detector also rotates about the vertical axis in the plane of the figure, but the angular displacement is twice that of the sample to maintain the angular correlation of  $\theta$ – $2\theta$  between the sample and the rotation detector.

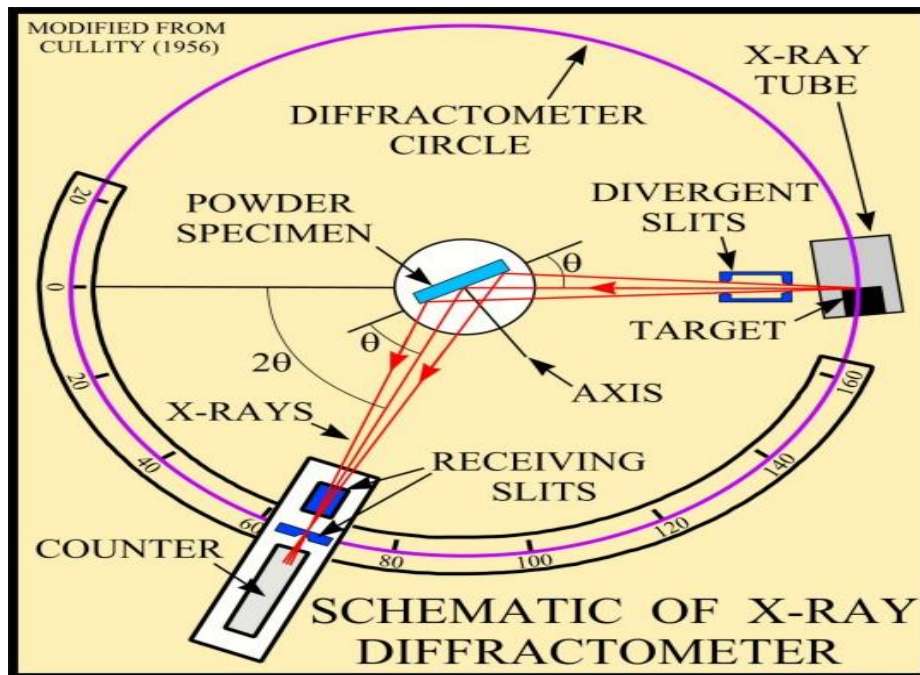


Figure 3.2: Geometric arrangement of x-ray diffractometer [72]

XRD patterns of Canadian asphalt binder have similarities and show at least 3 peaks which provide at least three maxima which could be seen at  $2\theta$  approximately, 002 graphene at  $25^\circ$  and  $44^\circ$  (10) band is a weak indicator of a broad peak (11) which is position in the middle at  $2\theta=80^\circ$  is seen. These broad features show that there is a partial ordering in the asphaltene. The distance median is indicated using the graphene band (002) maximum which is seen at of around  $25^\circ$  of the  $2\theta$  axis than the line the sheet aromatic of asphaltene that is calculated by a Bragg equation. The peak (002) is seen around  $2\theta=25^\circ$ , showing an interlayer spacing nearly about  $3.55^\circ$ . The peak (002) represents the space that exists between the condensed layers of the aromatic structure. As seen in the literature review, a single graphite crystal structure with an interlayer spacing of about  $3.35^\circ$  and an amorphous carbon which is an interlayer distance of about  $3.55^\circ$ . The value of  $d_m$  is associated with the thickness as well as the size of the aromatic sheets. The distance of the interlayer of the asphalt of the Canadian samples can be seen in the range of amorphous materials of small order. The average of the distance between the saturated portions (aliphatic chains, condensed saturated rings) molecules or interchain layer distance is given by the relationship:

$$d_\gamma = (5 \lambda) / 8 \sin \theta. \quad (3.1)$$

where  $d_\gamma$  is the interchain layer distance and  $(\lambda)$  is the wavelength of the  $CuK\alpha$  radiation (and  $\theta$  is the Bragg's angle).

The average height of the stack of aromatic sheets perpendicular to the sheet plane was determined using the following formula:

$$L_c = 0.9\omega \cos\theta = \frac{0.45}{B_{1/2}} . \quad (3.2)$$

Where  $\omega$  is the FWHM value obtained using the (002) band. The aromaticity of asphalt molecules  $f_a$  is calculated from the area (A) of resolve peaks for the ( $\gamma$ ) and graphene bands using the following equation:

$$f_a = \frac{A(002)}{A(002) + A\gamma} = \frac{C_A}{C_A + C_S} . \quad (3.3)$$

Where  $f_a$  is the percentage of carbon atoms in aromatic structures,  $C_A$  is the number of aromatic carbon atoms,  $C_S$  is the number of saturated carbon atoms,  $A(002)$  is the area of the graphene band, and  $A(\gamma)$  is the area of the ( $\gamma$ ) band. The distance between the aromatic sheets  $d_m$  was calculated according to Bragg's law using the following equation:

$$d_m = \frac{\lambda}{2\sin\theta} . \quad (3.4)$$

where  $d_m$  is the interlayer distance and ( $\lambda$ ) is the wavelength of the  $CuK\alpha$  radiation (and  $\theta$  is the Bragg's angle).

The average number of aromatic sheets in a stacked cluster  $M_e$  was calculated from the values of  $L_c$  and  $d_m$  by using the following equation:

$$M_e = \frac{L_c}{d_m} + 1 . \quad (3.5)$$

The diameter of the average layer in the aromatic sheets can be calculated by using the Scherrer's crystallite size equation in the following formula:

$$L_a = \frac{1.84\lambda}{\omega \cos\theta} = \frac{0.92}{B_{1/2}} . \quad (3.6)$$

where  $B_{1/2}$  is the full width at half maximum (FWHM) for the (11) band, and  $(\omega)$  is the bandwidth.

### 3.3 Sample preparation for XRD

The sample of the asphalt binder is prepared in a thin film on the side of the glass holder by heating up to 150°C for about 10 minutes in an oven and this followed by air cooling and removal from the atmosphere of the room. Table 3.1 shows the specimen collected from specific location and all the samples follow the PG standard set by CGSB.

Table 3. 1 Pertinent Asphalt Binder Properties

Asphalt Binders	Source	Modification Type	Grades
L3	Cold lake	Straight	PG 46-34
L5	unknown	Oxidized	PG 64-34
L6	unknown	straight	PG 64-28
L7	Cold lake	Straight (Hearst, Ontario)	PG 52-34
655-1	Unknown	SBS	PG 64-34

### 3.4 Method of thin film XRD

In this section, structure types will be defined to make it more appropriate to perform a suitable X-ray diffraction experiment. Generally, X-ray diffraction experiments are similar in that they produce a three-dimensional distribution of the intensity that reflects the three-dimensional nature of the material under investigation [73,74]. There are different special factors that need to be considered when using the sample of XRD thin film. A high angular resolution is needed to the fact that the peak from the semiconductor materials is very sharp because of the fact that the material has low defect densities. In addition, the numbers of monochromator crystals in multiple forms are used to give a very high collimated X-ray beam to the measurement. Before the XRD, each of the samples was put on one glass side and annealed at 150°C for about 10 minutes so to create a thin film that has a thickness of about 1mm. The X-ray measurement is run on a Rigaku D/Max-2200v-PC through the monochromatic Cu-K- $\alpha$  radiation operation at 40kV and 40mA. The category of the scan used is about 5-110°2 $\theta$  at a rate of 0.01/s and a time of 5 s/step. Samples were aged for one week and then analyzed at room temperature of 20°C. The width is at half maximum (FWHM), and the fit of the profile is obtained of a Pearson VII and pseudo-Voigt profile which have a background that is fixed ranging over 5 to 35°2 $\theta$  and 60 to 110°2 $\theta$ . The pattern of the X-ray creation and analysis were performed using a Jade version 6.1 software package incorporation the Pearson VII and pseudo-Voigt functions. The data that have been collected were normalized, and has a background that was common and compared the features using the four main peaks that were measured, i.e. gamma,

(002) graphene, (10) and (11). The diffraction of all X-rays used samples in an aluminum holder with dimension of 25 mm diameter and thickness of 1mm [75].

### 3.5 Instruments for X-ray thin-film measurements

In general, the X-ray diffractometer, which allows a wide range of measurements, is a complex instrument consisting of various components including a measurement axis, position adjustment axes, optical elements, and so on. Figure 3.3 shows X-ray thin-film diffractometer equipped with a  $2\Theta\chi$  axis.

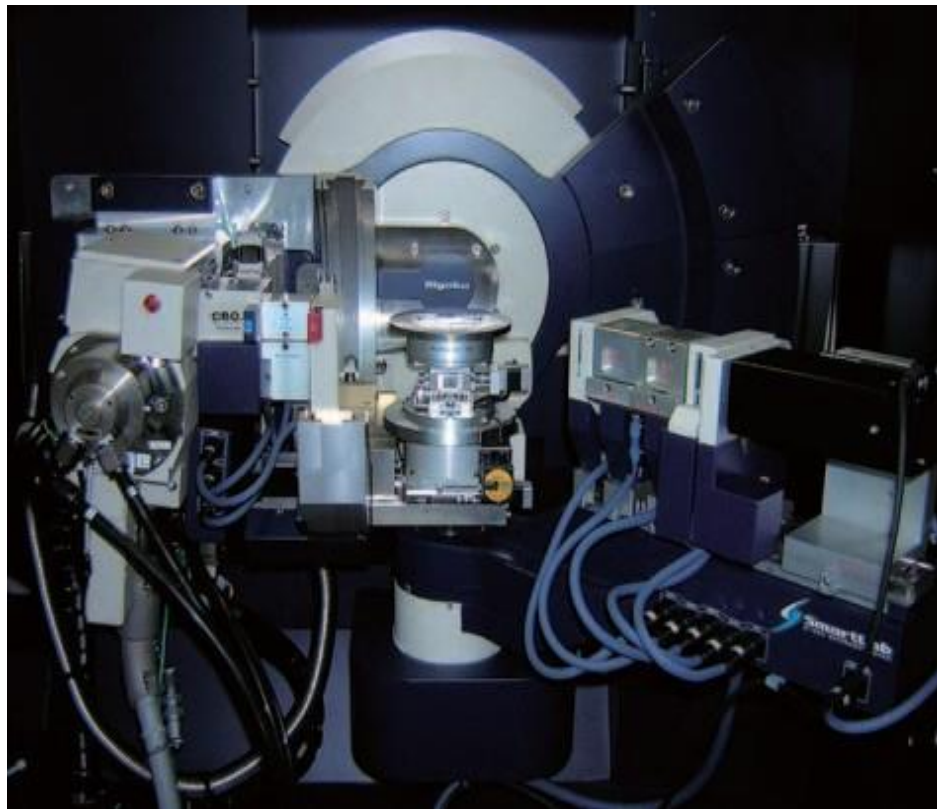


Figure 3.3: X-ray thin-film diffractometer equipped with a  $2\Theta\chi$  axis (SmartLab) [76].

### **3.6 Spectral Line Shapes Modeling Using Mathematical Functions**

The separation of the band (002) and gamma band in the manner seen above to determine the aromaticity and crystal size parameters

### **3.7 Line Shape Analysis Using Peak Search and Profile Fit**

The XRD spectra were peak searched using a parabolic filter (10,000 raw data points, screened out Ka-2 peaks, peak location summit, threshold sigma 3.0, intensity cutoff 0.1 percent, range to find background 1.0, points to average background 7) over the angular range of  $5^\circ$  to  $110^\circ$ .

The full width at half maximum (FWHM) and profile fits were obtained by using either Pearson VII or pseudo-Voigt function (fixed background, exponent = 0.6, 0.8, 1.2 and Lorentzian = 0.4, 0.7, 0.9) over the ranges  $5^\circ$  to  $35^\circ$   $2\theta$  and  $60^\circ$  to  $110^\circ$   $2\theta$  on the XRD line spectra of interest. The XRD spectra were also modeled in Mathematica using a generalized Fermi function (GFF).

## Chapter 4

### Results and Discussion

Four key peaks are present in the XRD patterns of the asphaltene binders (Gamma, (002) graphene, (10), (11)) just as Yen model describes it as shown in figure 2.3. The data From Table 4.1 show that the values of GFF range between  $f_a = 0.363$  to 0.96 and  $d_m = 4.795$  to 5.539 meaning that the profile fitting is not as consistent as P and V because XRD patterns are asymmetric.

#### 4.1 XRD Patterns

XRD patterns collected for the 5 asphalt binders were generated by standard processes as described in the Jade™ Software (version 6.1). The figures from (4.1) to (4.5) illustrate results for the asphalt samples (L3, L5, L6, L7, as well as 655-1).

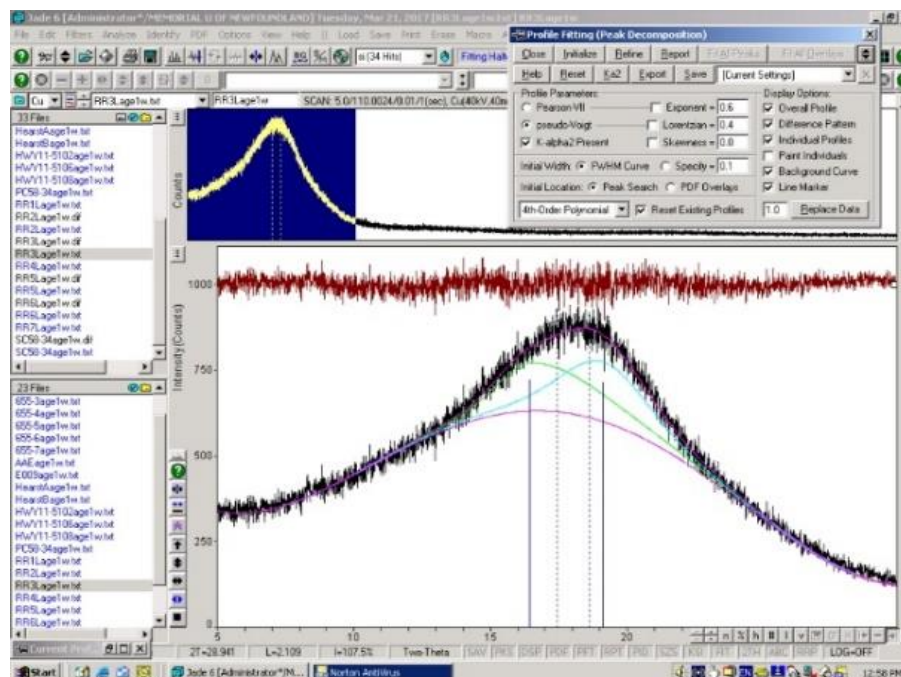


Figure 4.1a: Specimen L3 (4<sup>th</sup> order background, Lorentzian =0.4)

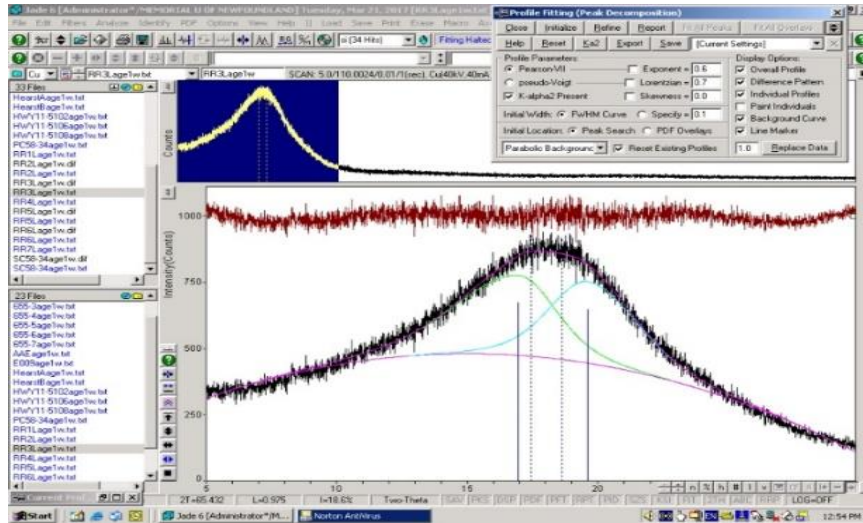


Figure 4.1b: Specimen L3 (parabolic background, Lorentzian =0.7)

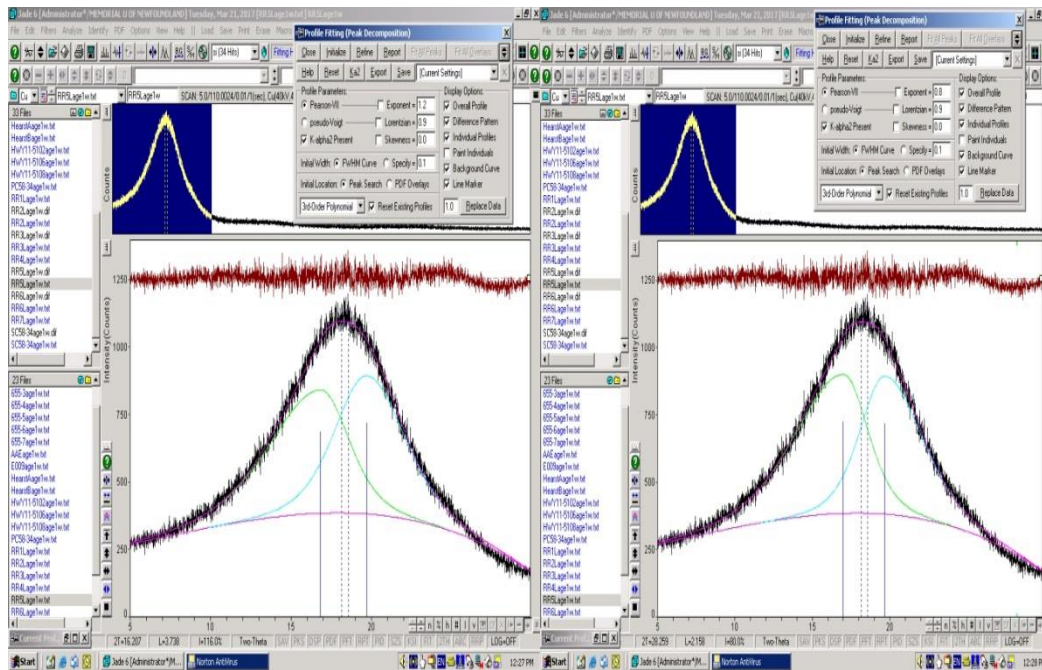


Figure 4.2: Specimen L5 (3<sup>rd</sup> Order Background, Lorentzian =0.9) and L5 of XRD (3<sup>rd</sup> Order Background, Lorentzian, Lorentzian =0.9)

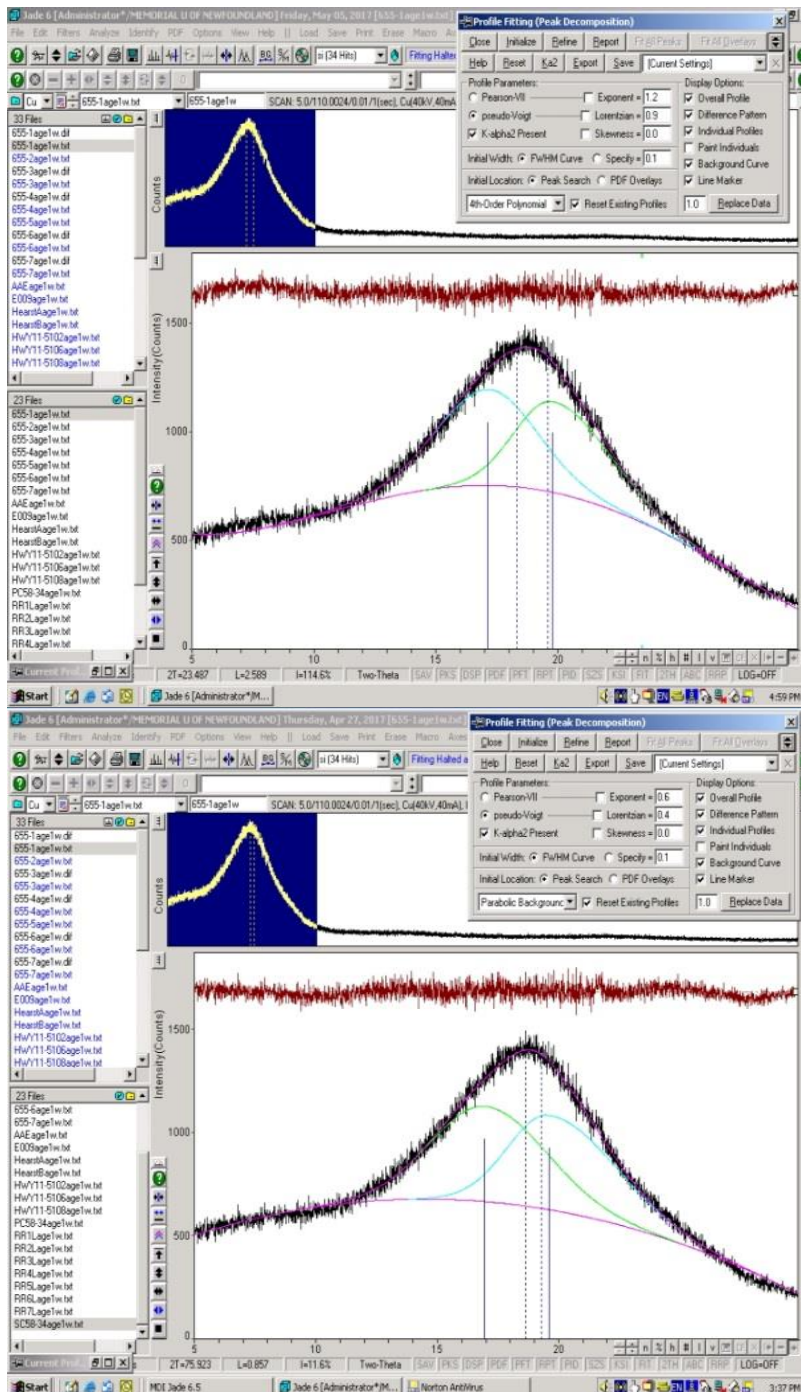


Figure 4.3: Specimen 655-1 (4<sup>th</sup> Order Background, Lorenzian =0.9) and 655-1 of XRD (Parabolic Background, Lorenzian =0.4)

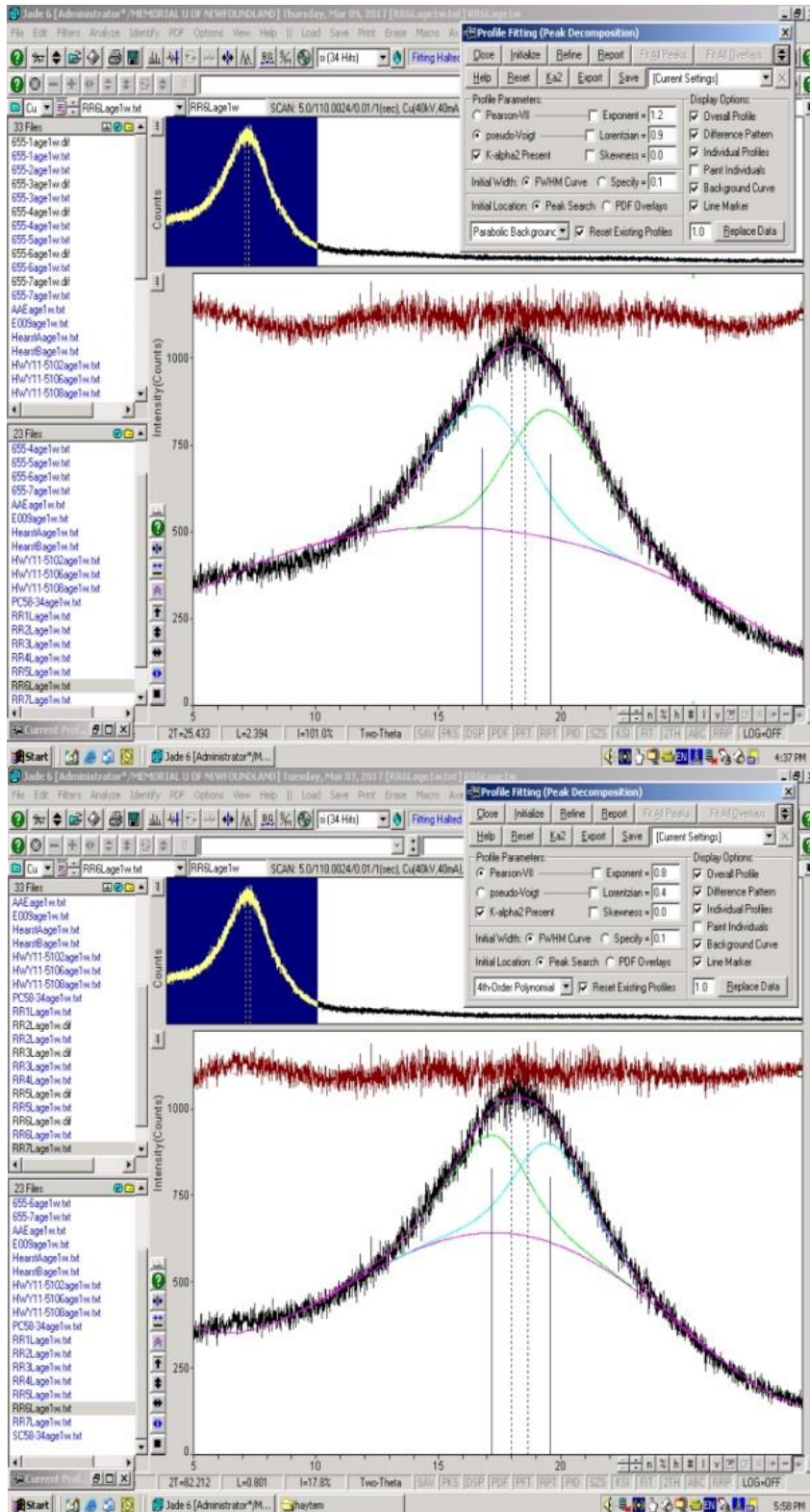


Figure 4.4: Specimen L6 (Parabolic Background, Lorentzian, Lorentzian =0.9) and L6 of XRD (4<sup>th</sup> Order Background, Lorentzian =0.4)

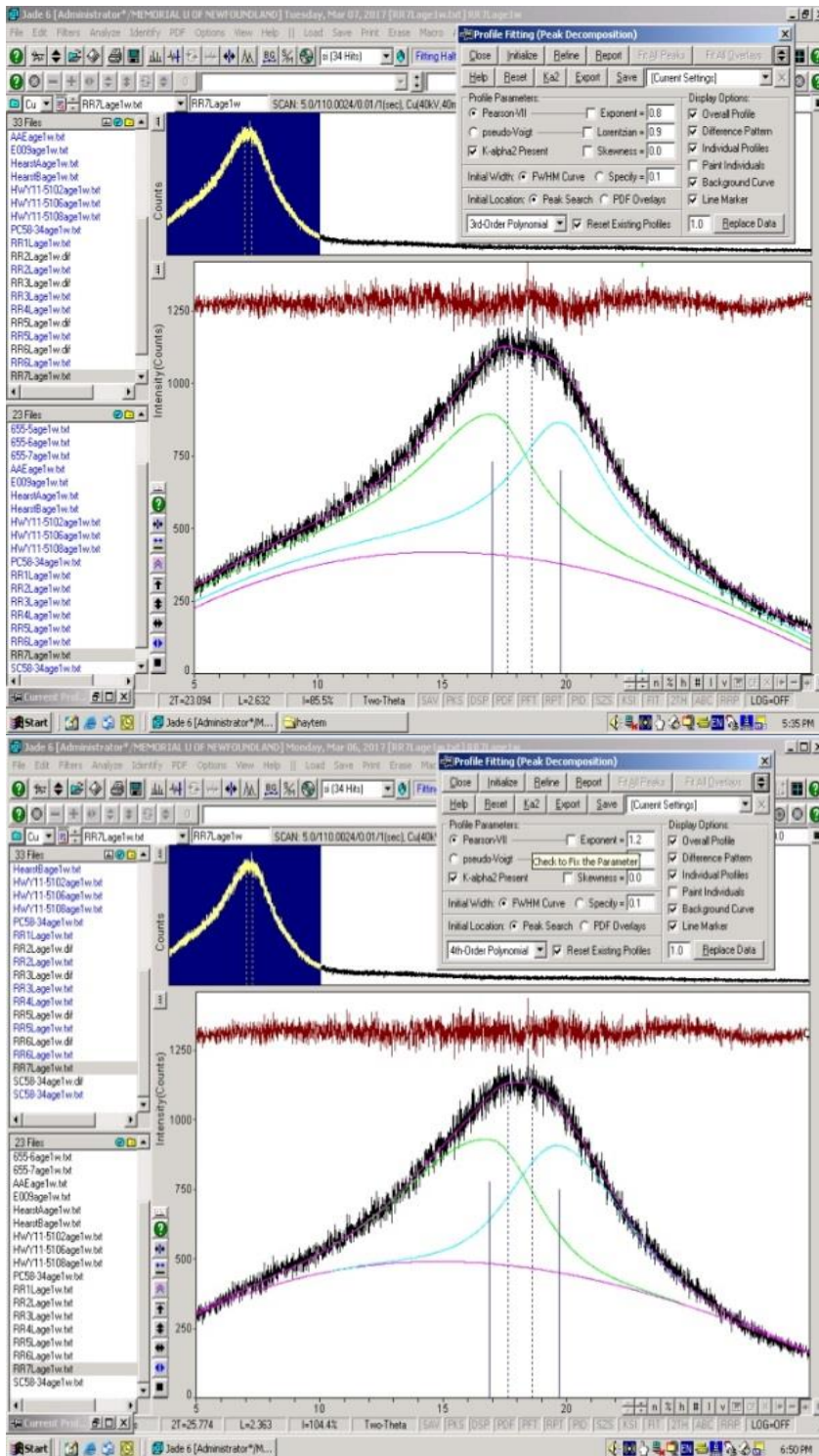


Figure 4.5: Specimen L7 (3<sup>rd</sup> Order Background, Lorenzian =0.9) and L7 of XRD (4<sup>th</sup> Order Background, Lorenzian =0.4)

## 4.2 XRD types with Different Backgrounds and Effect of Backgrounds

As shown in Figure 4.6, profile function that is either Pearson VII or pseudo-Voigt was used to fit the XRD data.

We will discuss the four different types of samples and data are fitted to obtain the best peaks, we initially use all backgrounds such as (Fixed, Level, Linear, Parabolic, 3<sup>rd</sup> order, 4<sup>th</sup> order). The samples which we worked on are (L3, L5, L6, and L7).

From the results, we found that the best backgrounds we used are (Parabolic, 3<sup>rd</sup> order, 4<sup>th</sup> order) because they are giving the obvious peaks for the ( $\gamma$ ) and (002) graphene. These are shown in figures (4.1 to 4.6). Table 4.1 shows the percent of error for the parameters ranging between 4.54 and 5.25, where the highest value is 1.2 at 4<sup>th</sup> order and less value is 4.54 at the 3<sup>rd</sup> order, for each of the Pearson VII and Pseudo-Voigt.

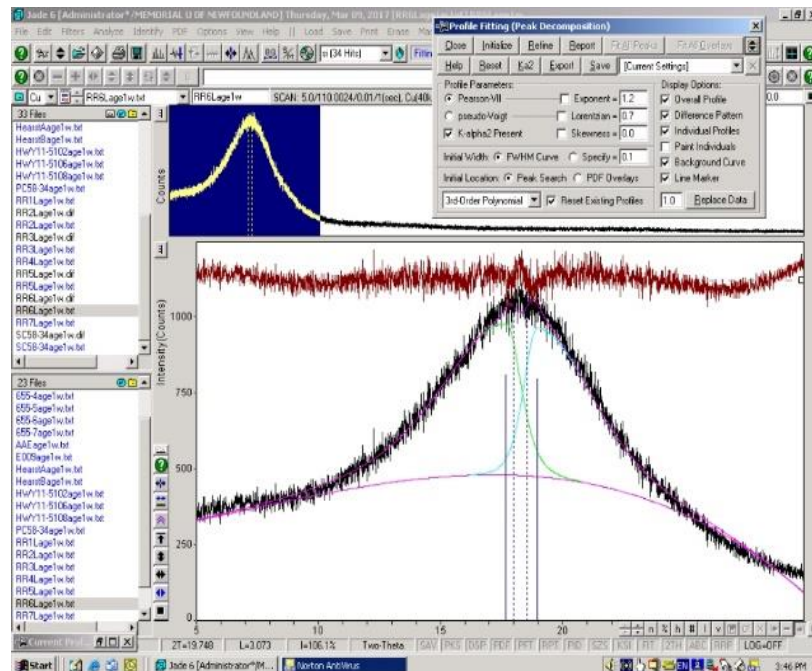


Figure 4.6: Profile fit of asphalt binder

### 4.3 Peak Shape Functions

As depicted in figures 4.1 to 4.6, we can locate the intensity,  $Y(i)$ , from the  $i$ th point's general form in the ( $1 \leq i \leq n$ ) diffraction pattern, with  $n$  representing all the measured points and being the contribution summation,  $y_k$ , of the  $m$  in each Bragg peak ( $1 \leq k \leq m$ ) and background,  $b(i)$  [77]:

$$Y(i) = b(i) + \sum_{k=1}^m I_k [y_k(x_k) + 0.5y_k(x_k + \Delta x_k)]. \quad (4.1)$$

where  $I_k$  represents the  $k$ th Bragg reflection intensity,  $x_k = 2\theta_i - 2\theta_k$ , and  $\Delta x_k$  represents contrasts among  $K_{\alpha 1}$  and  $K_{\alpha 2}$  component Bragg angles in the XRD doublet  $\gamma$  and graphene (002) in asphalt binders.

By applying the Bragg intensity in this equation as a multiplier, we can analyze the behaviors of a variety of normalized functions without deferring to peak intensity. In other words, we make the assumption that, for each case, the peak shape function's definite integral (working from negative to positive infinity) is unity. Based on this approach, we define 4 typical empirical peak shape functions ( $y$ ) as below:

$$y(x) = \textit{pseudo - voigt} = \eta \frac{C_G^{1/2}}{\sqrt{\pi}H} \exp(-C_G x^2) + (1 - \eta) \frac{C_L^{1/2}}{\pi H'} (1 + C_L x^2)^{-1} \quad (4.2)$$

where  $H$  and  $H'$  indicate FWHM.

Pearson-VII:

$$y(x) = PVII(x) = \frac{\Gamma(\beta)}{\Gamma(\beta-\frac{1}{2})} \frac{C_P^{1/2}}{\sqrt{\pi H}} (1 + C_P x^2)^{-\beta}. \quad (4.3)$$

GFF: Generalized Fermi Function

$$h(s) = \frac{A}{\exp(-a(s - c)) + \exp(b(s - c))}. \quad (4.4)$$

where a, b and c are represented the parameters described as  $s = \frac{2\sin\theta}{\lambda}$ , and A and c values represent the fit's amplitude and position. Meanwhile, a and b represent the fit's control shape.

$$X = \frac{(2\theta_i - 2\theta_k)}{H_k}. \quad (4.5)$$

where (X) is the XRD Bragg angle of the ith point in the diffraction pattern with its origin in the position of kth peak divided by the peak's FWHM.  $(2\theta_i)$ , is the Bragg angle of the ith point of the diffraction pattern.  $(2\theta_k)$ , is the Bragg angle of the kth Bragg reflection [35].

$C_G = 4\ln 2$ , while  $\frac{\sqrt{C_G}}{\sqrt{\pi H}}$  indicates the Gauss function normalization factor as: [77]

$$\int_{-\infty}^{\infty} \frac{\sqrt{C_G}}{\sqrt{\pi H}} \exp(-C_G x^2) dx = 1. \quad (4.6)$$

$C_L = 4$ , while  $\frac{\sqrt{C_L}}{\pi H'}$  indicates the Lorentz function normalization factor as:

$$\int_{-\infty}^{\infty} \frac{\sqrt{C_L}}{\pi H'} \exp(1 + C_L x^2)^{-1} dx = 1. \quad (4.7)$$

$C_p=4(2^{1/\beta} - 1)$ , and  $[\frac{\Gamma_\beta}{\Gamma_{(\beta-1/2)}}] \frac{\sqrt{C_p}}{\sqrt{\pi H}}$  are the Pearson VII function normalization

factors as follows: [77]

$$\int_{-\infty}^{\infty} [\frac{\Gamma_\beta}{\Gamma_{(\beta-1/2)}}] \frac{\sqrt{C_p}}{\sqrt{\pi H}} \exp(1 + C_p x^2)^{-\beta} dx = 1. \quad (4.8)$$

$$H = (U \tan^2 \theta + V \tan \theta + W) / 2. \quad (4.9)$$

The Caglioti formula (above) shows that the FWHM as a function of  $\theta$  for Gauss, Pearson VII, Pseudo-Voigt functions. U, V, and W are free variables [77].

$$H' = \frac{U}{\cos \theta} + V \tan \theta. \quad (4.10)$$

where  $H'$  represents the FWHM function of ( $\theta$ ) in the Lorentz function and U, V indicates free variables.

$$\eta = \eta_0 + \eta_1 2\theta + \eta_2 \theta^2. \quad (4.11)$$

where,  $0 \leq \eta \leq 1$ , while  $\eta$  represents a mix parameter for the Pseudo-Voigt function. In other words, it is the Gauss function's fractional contribution as part of the combined linear Gauss and Lorentz functions, where  $\eta_0$ ,  $\eta_1$  and  $\eta_2$  indicate free variables.

$$\beta = \beta_0 + \frac{\beta_1}{2\theta} + \frac{\beta_2}{2\theta^2}. \quad (4.12)$$

where  $\beta$  Indicates the exponent working as a Bragg angle function as part of the Pearson-VII functions, while  $\beta_0$ ,  $\beta_1$  and  $\beta_2$  represents are free variables.

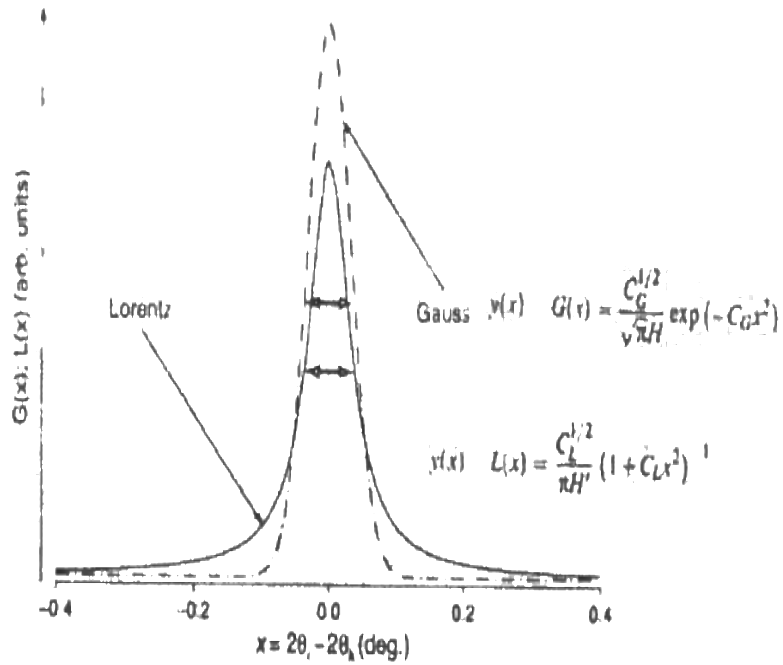


Figure 4.7: Gauss and Lorentz peak shape functions [48]

Figure 4.7 depicts the peak shape functions for both Gauss (dashed-dotted line) and Lorentz (solid line) peak shape functions, while the FWHM is represented by thick horizontal arrows.

As can be seen, the two peak shape functions that are least complex are Gaussian and Lorentzian distributions working from Bragg peak intensities. Moreover, the Lorentz function shows a sharp peak close to the maximum, with lengthy “streams” flowing on both sides close to the base. Conversely, the Gauss function around maximum and shows no such streams. Nonetheless, both functions can be described as centrosymmetric, in that:  $G(x) = G(-x)$  and  $L(x) = L(-x)$ .

The formation of real Bragg peaks is an outcome derived from functions ranging from convoluting multiple instrumental to specimen functions. However, they cannot be adequately described in XRD as Gaussian and Lorentzian distributions. Because peak shapes typically occur among these distributions, they can most accurately be described using a mix of the two, such as, for instance convoluting the Gauss and Lorentz methods as a variety of proportions. Convolution, however, can be a complicated process involving numerical integration if any of the peak shape function parameters are modified. Thus, an easier version Gauss and Lorentz linear combination – Pseudo-Voigt – can be applied. In this pared-down approach, we mix Gaussian and Lorentzian compounds ( $\eta$  to  $1-\eta$  ratio) until the mixing parameter value of ' $\eta$ ' shifts to 1 Gauss from 0 Lorentz, keeping in mind that beyond this range in this formulation,  $\eta$  has no meaning. An additional peak shape function that can be applied is the Pearson VII, as presented in Eq. (4.3).

A brief examination reveals that this is very much like the Lorentz distribution, other than for the fact that the exponent ( $\beta$ ) in Pearson VII can be variable but stays the same ( $\beta= 1$ ) in Lorentz. Specifically, Pearson VII offers intensity distribution similar to Pseudo-Voigt, in that when ( $\beta = 1$ ), it is the same as the Lorentz distribution; furthermore, when ( $\beta \cong 10$ ), the Gaussian and Pearson VII functions are equal. So, if exponents are  $0.5 < \beta < 1$  or  $\beta > 10$ , the peak shape exceeds, respectively, the Lorentz and Gauss functions. That being said,  $\beta$  values only very rarely occur.

Figure 4.1-4.6 illustrates XRD profile-fitting employing Pearson VII. However, the Pearson VII and Pseudo-Voigt functions are depicted as symmetrical. Peak maximum is calculated from the argument,  $x$ , in the four empirical functions, as follows:

$$x = 0 \text{ and } 2\theta_i = 2\theta_k.$$

Therefore, peak FWHM at a  $2\theta$  can be given as in Eq. (4.13):

$$\text{FWHM} = H = \sqrt{U \tan^2 \theta + V \tan \theta + W}. \quad (4.13)$$

The “H” in FWHM is another parameter that can help find the argument’s value, which can change with  $2\theta$ . Being Bragg angle-dependent, the H can be depicted as a function related to empirical peak-broadening. As such, it includes 3 free parameters (namely,  $U$ ,  $V$ ,  $W$ ), but the Lorentzian has only 2.

#### 4.4 Samples figures with GFF

The following figures corresponding to 4 of the 5 samples (L3, L5, L6, and L7) of the GFF profile fits from XRD data are shown below. The four peaks in the figures represent the  $\gamma$ , (002) graphene, (10), and (11) [ the latter correspond to the (100) and (110) planes] are the same as found in the XRD patterns.

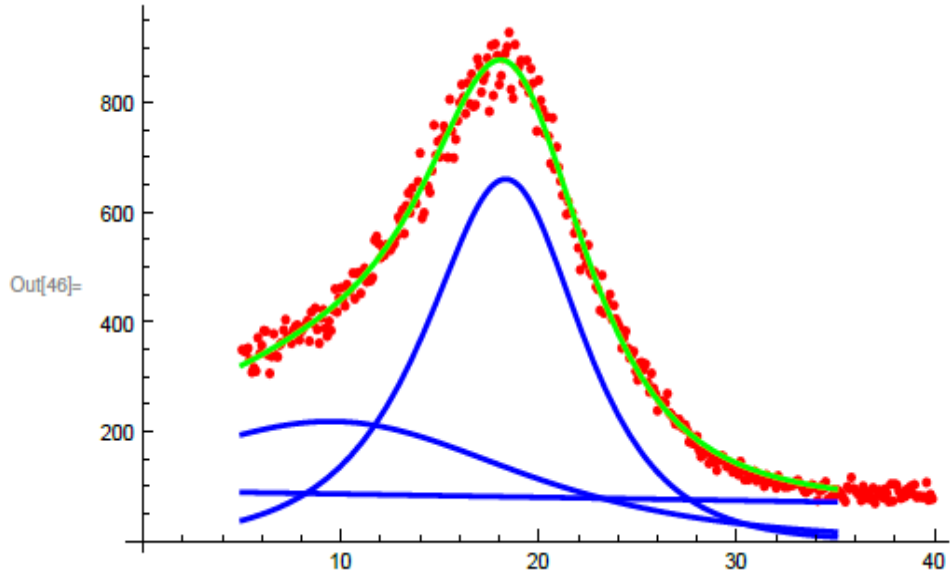


Figure 4.8: Sample L3 from GFF

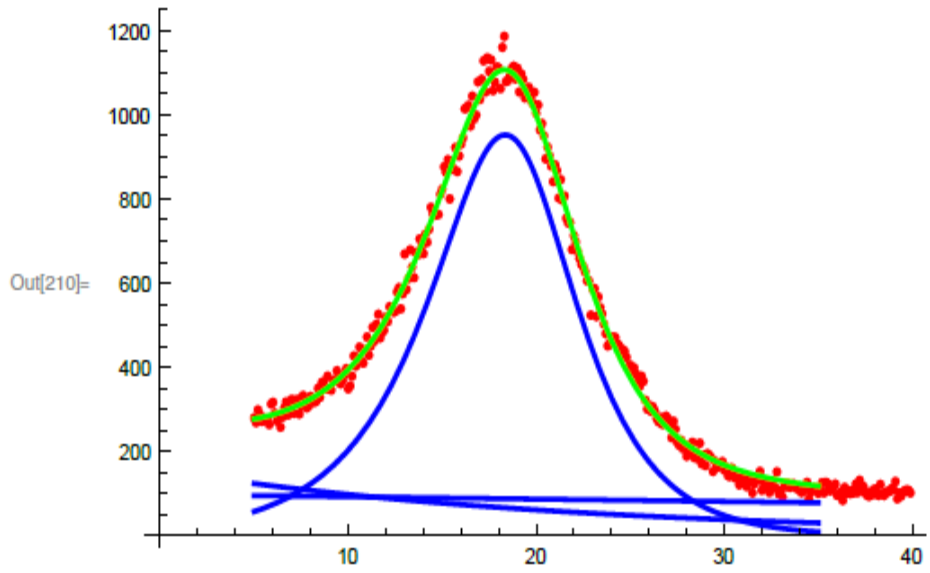


Figure 4.9: Sample L5 from GFF

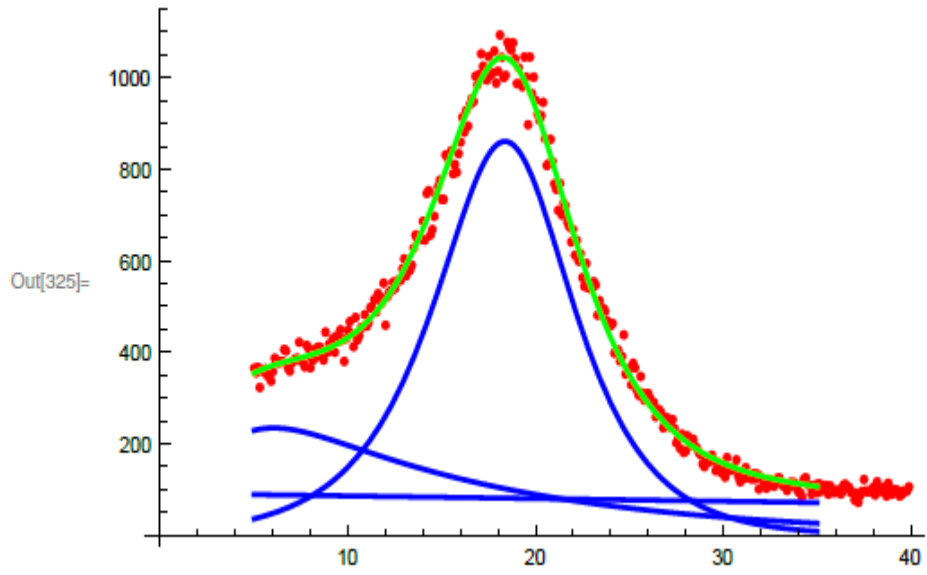


Figure 4.10: Sample L6 from GFF

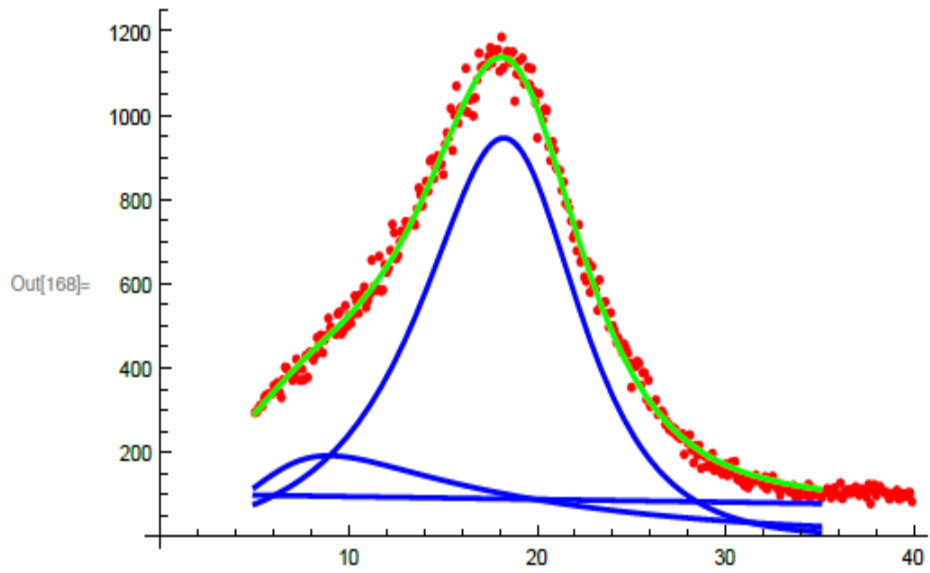


Figure 4.11: Sample L7 from GFF

#### 4.5 Comparing the Results of all Asphalt Samples

The observed X-ray diffraction patterns need fitting of the theoretical distributions that are very important to acquire information the spectral lines. Pseudo-Voigt and Pearson-VII fitting procedures are employed, and the 3 main bands  $\gamma$ , (002), and (10) cited at approximately  $2\theta = 20^\circ$ ,  $25^\circ$ , and  $44^\circ$  were employed as the first estimates.

It is possible to observe the (004) band on the high  $2\theta$  side in some situation at  $2\theta$  at approximately  $53^\circ$ . Also, by estimating the intensity and peak width, the regression can be initiated. On the other hand, on the low  $2\theta$  side the baseline is not sufficiently well defined. So, one ought to use the high value end of the XRD pattern and fix this as a steady baseline. This introduces the possibility for a sensible assumption, inspired assumption, of statistical inaccuracies that may impact the result for the operator. It's important to know that the background of the samples has a big effect on the results. As we can see from the table 4.1 the 3<sup>rd</sup> order and Parabolic Background have the best results, meanwhile, the 4<sup>th</sup> order has weak  $L_c$  and  $L_a$ . Some of the data have similar result in an aromaticity such as L5, L7 with Parabolic and 3<sup>rd</sup> order background respectively. In other hand, the samples with 4<sup>th</sup> order background have different results.

Meanwhile, for the low  $2\theta$  side, because the baseline cannot yet be accurately defined, the XRD pattern's high value must, by default, be applied as the baseline. However, the process then involves errors arising from reasonable assumption and/or statistical inaccuracies, both of which can skew results. It is

worth noting that alterations in the baseline generally had no or only a very minor impact on results related to factors like aromaticity

Table 4.1: The Aromaticity and Crystallite Parameters Calculated with the use of Pearson VII, Pseudo-Voigt, and GFF

Sample	Background	Exp	Lor	Error%
RR3L	4 <sup>th</sup> order	0.6	0.4	4.82
	4 <sup>th</sup> order	0.8	0.7	4.85
	4 <sup>th</sup> order	1.2	0.9	4.70
	parabolic	0.6	0.4	4.89
RR5L	parabolic	0.8	0.7	5.10
	parabolic	1.2	0.9	5.28
	4 <sup>th</sup> order	0.6	0.4	5.25
RR6L	4 <sup>th</sup> order	0.8	0.7	4.8
	4 <sup>th</sup> order	1.2	0.9	4.93
	3 <sup>rd</sup> order	0.6	0.4	4.54
RR7L	3 <sup>rd</sup> order	0.8	0.7	4.73
	3 <sup>rd</sup> order	1.2	0.9	4.56

Table 4.2: The Aromaticity and Crystallite Parameters Calculated with the use of Pearson VII, Pseudo-Voigt, and GFF

Sample	f <sub>a</sub>			d <sub>m</sub>			d <sub>γ</sub>			L <sub>c</sub>			L <sub>a</sub>			M <sub>e</sub>		
	p7	v	gf	P7	V	GF	P7	V	GF	P7	V	GF	P7	V	GF	P7	V	GF
RR3L	4.6	4.6	5.5	6.9	6.7	6.1	6.5	6.8	3.2	13.3	13.9	6.6	2.4	2.5	1.6	4.6	4.6	5.5
	4.6	4.6	5.5	6.6	6.8	6.1	7.1	6.7	3.2	14.5	13.6	6.6	2.6	2.4	1.6	4.6	4.6	5.5
	4.6	4.7	5.5	6.6	6.9	6.1	7.3	6.4	3.2	15.0	13.1	6.6	2.6	2.4	1.6	4.6	4.7	5.5
	4.4	4.5	5.4	6.3	6.5	5.9	4.3	4.6	3.1	8.7	9.4	6.4	2.0	2.0	1.6	4.4	4.5	5.4
RR5L	4.5	4.6	5.4	6.4	6.6	5.9	5.0	4.2	3.1	10.1	8.6	6.4	2.1	1.9	1.6	4.5	4.6	5.4
	4.5	4.4	5.4	6.4	6.4	5.9	4.9	5.1	3.1	10.1	10.4	6.4	2.1	2.2	1.6	4.5	4.4	5.4
	4.5	4.5	4.8	6.3	6.4	5.3	7.0	6.6	2.8	14.2	13.5	5.7	2.5	2.5	1.6	4.5	4.5	4.8
RR6L	4.5	4.5	4.8	6.4	6.4	5.3	7.0	6.6	2.8	14.2	13.5	5.7	2.5	2.5	1.6	4.5	4.5	4.8
	4.5	4.6	4.8	6.4	6.7	5.3	6.8	6.6	2.8	13.8	13.4	5.7	2.5	2.4	1.6	4.5	4.6	4.8
	4.5	4.3	5.2	6.5	6.3	5.7	4.3	4.2	3.0	8.8	8.5	6.2	2.0	2.0	1.6	4.5	4.3	5.2
RR7L	4.4	4.5	5.2	6.5	6.3	5.7	5.0	4.3	3.0	10.2	8.8	6.2	2.1	2.0	1.6	4.4	4.5	5.2
	4.5	4.4	5.2	6.6	6.5	5.7	4.2	4.3	3.0	8.7	8.8	6.2	1.9	2.0	1.6	4.5	4.4	5.2
	4.6	4.6	5.5	6.9	6.7	6.1	6.5	6.8	3.2	13.3	13.9	6.6	2.4	2.5	1.6	4.6	4.6	5.5

Table 4.2 shows the results from calculation of aromaticity ( $f_a$ ) and crystallite parameters (the interlayer distance between the aromatic sheets  $d_m$ , the interchain layer distance  $d_\gamma$ , the diameter of the aromatic sheets  $L_a$ , the height of the stack of aromatic sheets  $L_c$ , and the number of aromatic sheets  $M_c$ ) for Pearson VII (P) varying exponent (0.6, 0.8, 1.2), pseudo-Voigt (V) varying Lorentzian (0.4, 0.7, 0.9), and Generalized Fermi (GF) Function in 5 samples. However, analysis of aromaticity and crystallite size parameters using the XRD data were sometimes mixed due to asymmetry in the GFF data and differences in calculating background intensity. In general, the results in XRD and GFF modeling are approximate there is a little difference between GFF values and Pearson VII and pseudo-Voigt values in  $L_a$  values and  $L_c$  values.

Aromaticity ( $f_a$ ) of approximately values 0.36 for L6 and 0.96 for L5 using GFF shows that the data fits were found to be very weak. L6 has a lower value, and L5 has the highest value in GFF function. For example, asphalt L6 from the presence of the XRD profile, as apparently having a large (002) contribution. Nevertheless, when we were using GFF the peak become very wide, and hence the (002) contribution become very small, making the aromaticity in the amount of only 0.36, while the Pseudo-Voigt and Pearson VII gave consistent aromaticity of approximately 0.50 and 0.49 respectively.

The same situation, when we see asphalt L7, having a  $f_a$  of about 0.86 when fitted in GFF, and 0.46 and 0.52 are obtained when we were using the same procedure for Pearson VII and Pseudo-Voigt functions.

In some instance, the (001) band can be found at the (10) peak's high  $2\theta$  side, positioned at around  $53^\circ$ . Also required to start the regression process are rough estimates of the peak width and intensity. Furthermore, as backgrounds can cause major problems in XRD patterning of asphaltenes, they could only be presented as a “best fit”. Figures below show comparison between different backgrounds and functions for the samples.

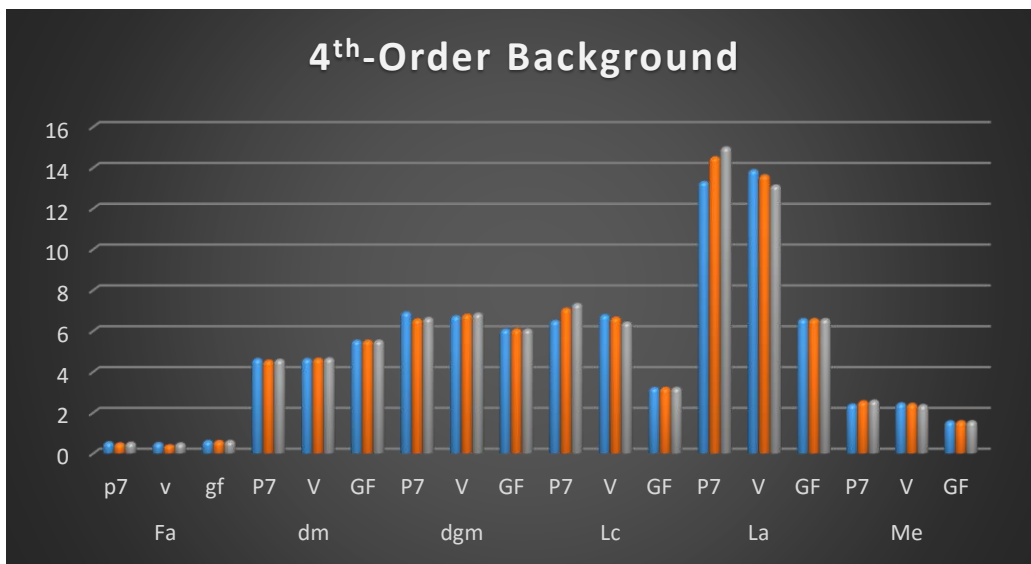


Figure 4.12: Aromaticity and crystallite parameters sample L3 calculated using Pearson VII, pseudo-Voigt and GFF (4<sup>th</sup> order background)

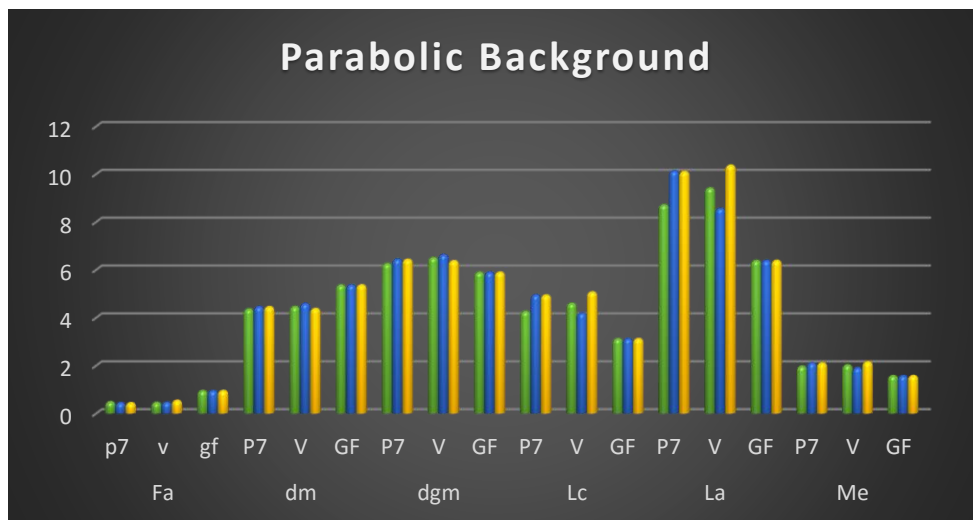


Figure 4.13: Aromaticity and crystallite parameters sample L5 calculated using Pearson vii, pseudo-Voigt and GFF (parabolic background)

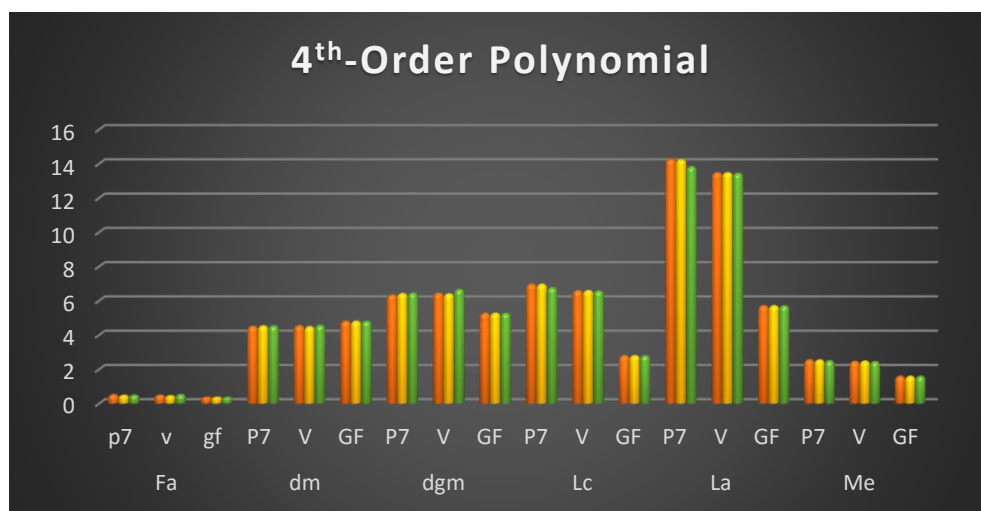


Figure 4.14: Aromaticity and crystallite parameters sample L6 calculated using Pearson vii, pseudo-Voigt, and GFF (4<sup>th</sup> order background)

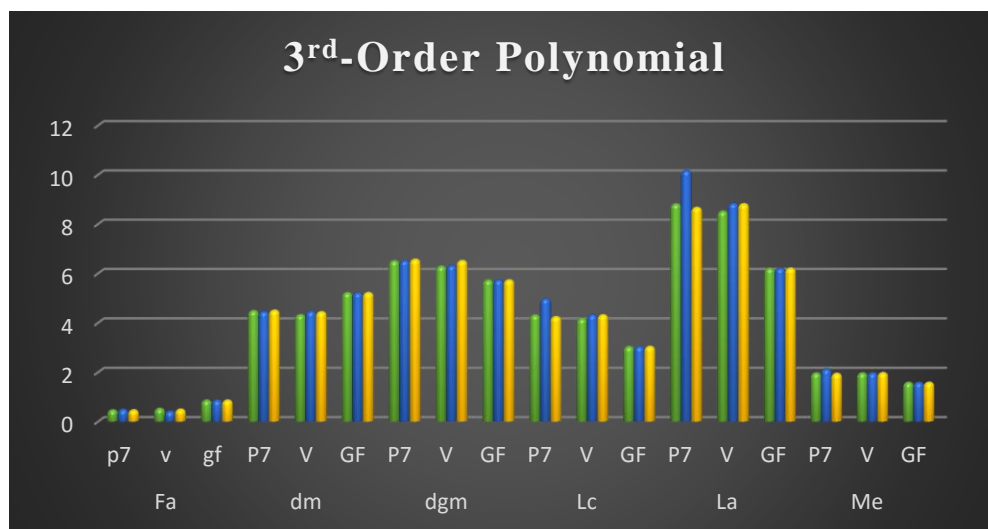


Figure 4.15: Aromaticity and crystallite parameters sample L7 calculated using, pseudo-Voigt and GFF (3<sup>rd</sup> -order background)

However, when using GFF the  $\gamma$  peak becomes very broad and hence the (002) contribution becomes very small. In addition, using the crystallite parameter of the interlayer distance ( $L_c$ ,  $L_a$ ) had much higher value of GFF in some samples compared to other samples from Pearson VII and pseudo-Voigt. However, the rest of the results for all other samples show more consistency. The higher aromaticity values for L5 and L7 indicates that distorted X-ray diffraction pattern at low angles that has a strong impact on the quality of the fit. For the rest of the samples, attempts at fitting an individual peak gave an aromaticity with approximately similar results with an error of  $\pm 0.1$ .

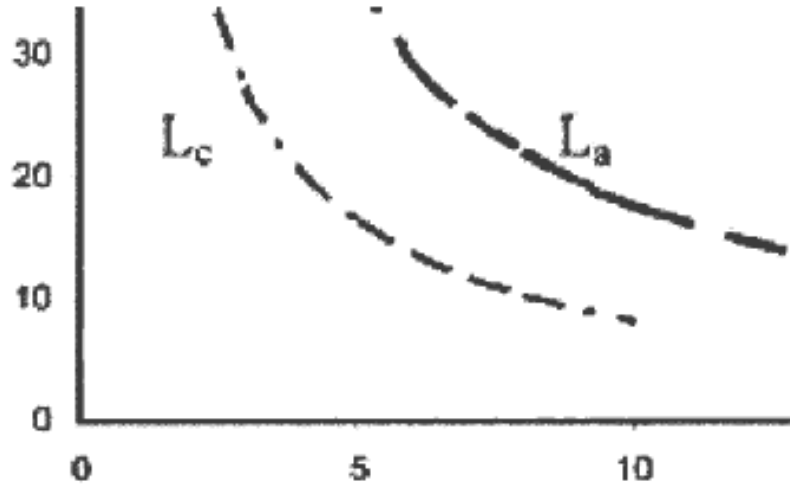


Figure 4.16: Modified figure of relationship showing crystalline dimension (vertical) versus bandwidth (horizontal) [48]

From Figure 4.5, we can assert that the two key parameters for finding crystallite size are  $L_c$  and  $L_a$ , despite their sensitivity to FWHM. Specifically,  $L_c$  shows sensitivity to even minor alterations in  $\gamma$ , such as, for instance, modifying  $2\theta = 5^\circ$  to  $2\theta = 6^\circ$  cuts the height of the stack in half (i.e., 1.5 nm from 3.0 nm). However, data involving sheet diameter appear to be not quite as sensitive; the only parameter affected seems to be the narrow (10) band. At the same time, we can assert that the results differ significantly even terms of trends if the research uses XRD and shifts between Pearson VII and Pseudo-Voigt. As shown in detail in the previous chapter, the fitting procedure can fall victim to hyper-simplification, as graphs generally require non-symmetric (002) peaks to be created through a number of different factors (e.g., noise in the data residue).

## Chapter 5

### Conclusion

Three major functions, which are Pearson VII, Pseudo-Voigt, and Generalized Fermi function (GFF) were used to compare XRD pattern profile fits. Jade™ XRD software were used with Pearson VII, and Pseudo-Voigt to calculate and compare crystallite size and aromaticity values. In addition, Mathematica was used to model the XRD data by using a generalized Fermi function with varied results comparable to Pearson VII, Pseudo-Voigt functions.

The asphalt binder samples were aged for one week. With the passage of time, XRD peaks showed that crystallinity increased in tandem with asphalt binder aging. Moreover, even small modifications of profile angles resulted in shifts in atoms in the planes, thus indicating a direct association between Pseudo-Voigt and Pearson VII functions, as well as GFF.

The discoveries of this present investigation highlight the expanding capacity of XRD to precisely depict the properties (which are auxiliary and compositional in nature) in binders of asphalt. The results discovered all vital for getting a handle on how pavements and asphalt binders age in a true setting. For that reason, extra research is needed to be done in this field, first by identifying the potential issues and then determine the additional research to address the issues.

## **Recommendations for Future Work**

As the challenges elevate to extract materials in their purest form, such as asphaltene, a new way of designing techniques should be implemented to improve the productivity and durability of materials. Develop mix designs for high-modulus asphalt mixes, including the selection of binder, optimum asphalt content for low voids, and required stiffness. Develop an understanding of pavement layer bonding. From both a construction and a performance standpoint, it is crucial to understand how bonding occurs between pavement layers and its role in pavement responses to loads, by studying the structure and composition of the mix samples at microscopic level.

## References

1. California. Ihueze, C. C., Ekwueme, O. G., Obuka, N. S., & Ogbodo, I. F. (2012). Evaluation of Optimum Asphalt Yield of a Process. *Evaluation*, 2(6).
2. Speight, J. G. (2015). *Asphalt Materials Science and Technology*. Butterworth-Heinemann.
3. <http://www.crisdel.com/blog/5-types-asphalt-pavement>
4. <https://www.thebalance.com/hot-mix-asphalt-types-844575>
5. <http://kleencoconstruction.com/news/cold-mix-asphalt-faq-cold-mix-asphalt/>
6. Sheu, E. Y. (2002). Petroleum asphaltene properties, characterization, and issues. *Energy & Fuels*, 16(1), 74-82
7. Pereira, J. C., López, I., Salas, R., Silva, F., Fernández, C., Urbina, C., & López, J. C. (2007). Resins: the molecules responsible for the stability/instability phenomena of asphaltenes. *Energy & Fuels*, 21(3), 1317-1321.
8. Heukelom, W. (1966, February). Observations on the rheology and fracture of bitumens and asphalt mixes. In *Assoc Asphalt Paving Technol Proc*.
9. Taha, R., Al-Harthy, A., Al-Shamsi, K., & Al-Zubeidi, M. (2002). Cement stabilization of reclaimed asphalt pavement aggregate for road bases and subbases. *Journal of Materials in Civil Engineering*, 14(3), 239-245.
10. Praticò, F. G., Casciano, A., & Tramontana, D. (2010). Pavement life-cycle cost and asphalt binder quality: Theoretical and experimental investigation. *Journal of Construction Engineering and Management*, 137(2), 99-107.

11. Moschopedis, S. E., Fryer, J. F., & Speight, J. G. (1976). Investigation of asphaltene molecular weights. *Fuel*, 55(3), 227-232.
12. Petroleum crude oil characterization by IMS-MS and FTICR MS. *Analytical chemistry*, 81(24), 9941-9947
13. Mayor, Agrawala. (2001) "Measurement and modeling of Asphaltene Association. "thesis Submitted to the Faculty of Graduate Studies in Partial Fulfillment of the Requirements for the degree of Master of Science in Chemical Engineering.Calgary, Alberta.Pg1.<http://www.CollectionsCanada.gc.C/obj/S4/fs/lsk3/ftp05/mg64992.pdf>
14. Kuznicki, T., Masliyah, J. H., & Bhattacharjee, S. (2008). Molecular dynamics study of model molecules resembling asphaltene-like structures in aqueous organic solvent systems. *Energy & Fuels*, 22(4), 2379-2389.
15. Dickie, J. P., & Yen, T. F. (1967). Macrostructures of the asphaltic fractions by various instrumental methods. *Analytical Chemistry*, 39(14), 1847-1852.
16. Liao, Z., Zhao, J., Creux, P., & Yang, C. (2009). Discussion on the structural features of asphaltene molecules. *Energy & Fuels*, 23(12), 6272-6274.
17. McKenna, A. M. (2009). Detailed characterization of heavy crude oils and asphaltenes by ultrahigh resolution Fourier transform ion cyclotron resonance mass spectrometry. The Florida State University.
18. Rogel, E., & Carbognani, L. (2003). Density estimation of asphaltenes using molecular dynamics simulations. *Energy & Fuels*, 17(2), 378-386.21.

19. Yarranton, H. W., & Masliyah, J. H. (1996). Molar mass distribution and solubility modeling of asphaltenes. *AIChE Journal*, 42(12), 3533-3543.
20. Stephenson, W. K. (1990). Producing asphaltenic crude oils: problems and solutions. *Petr. Eng. Int*, 8, 24-31.
21. Yarranton, H. W., Alboudwarej, H., & Jakher, R. (2000). Investigation of asphaltene association with vapor pressure osmometry and interfacial tension measurements. *Industrial & Engineering Chemistry Research*, 39(8), 2916-2924.
22. Sheu, E. Y., Storm, D. A., & Shields, M. B. (1995). Adsorption kinetics of asphaltenes at toluene/acid solution interface. *Fuel*, 74(10), 1475-1479.
23. Khristov, K., Taylor, S. D., Czarnecki, J., & Masliyah, J. (2000). Thin liquid film technique—application to water–oil–water bitumen emulsion films. *Colloids and Surfaces A: Physicochemical and Engineering Aspects*, 174(1), 183-196.
24. Gafonova, O. V., & Yarranton, H. W. (2001). The stabilization of water-in-hydrocarbon emulsions by asphaltenes and resins. *Journal of Colloid and Interface Science*, 241(2), 469-478.
25. Taylor, S. D., Czarnecki, J., & Masliyah, J. (2002). Disjoining pressure isotherms of water-in-bitumen emulsion films. *Journal of colloid and interface science*, 252(1), 149-160.28.
26. Adams, J. J. (2014). Asphaltene adsorption, a literature review. *Energy & Fuels*, 28(5), 2831-2856.
27. Wu, X. (2003). Investigating the stability mechanism of water-in-diluted bitumen emulsions through isolation and characterization of the stabilizing materials at the interface. *Energy & Fuels*, 17(1), 179-190.

28. Stanford, L. A., Rodgers, R. P., Marshall, A. G., Czarnecki, J., Wu, X. A., & Taylor, S. (2007). Detailed elemental compositions of emulsion interfacial material versus parent oil for nine geographically distinct light, medium, and heavy crude oils, detected by negative-and positive-ion electrospray ionization Fourier transform ion cyclotron resonance mass spectrometry. *Energy & Fuels*, 21(2), 973-981.
29. <http://www.pavementinteractive.org/materialsasphalt/>
30. Sharma, I. H., & Sharma, S. (2016). Cryogenic Processing of HSS M2: Mechanical Properties and XRD Analysis. In *MATEC Web of Conferences*(Vol. 57). EDP Sciences.
31. <https://www.xos.com/XRD>
32. <http://kasap13.usask.ca/EE271/files/XRayDiffraction.pdf>
33. Masad, E., Muhunthan, B., Shashidhar, N., & Harman, T. (1999). Internal structure characterization of asphalt concrete using image analysis. *Journal of computing in civil engineering*, 13(2), 88-95.
34. Harvey, J. T., Monismith, C. L., Nokes, W., & Coetzee, N. F. (2006). *Caltrans Partnered Pavement Research Program (PPRC) Summary Report: Four Year Period: 2000–2004*. Institute of Transportation Studies.
35. Mullins, O. C. (2010). The modified Yen model. *Energy & Fuels*, 24(4), 2179-2207.
36. Yarranton, H. W., Alboudwarej, H., & Jakher, R. (2000). Investigation of asphaltene association with vapor pressure osmometry and interfacial tension measurements. *Industrial & Engineering Chemistry Research*, 39(8), 2916-2924.

37. Sheu, E. Y., Storm, D. A., & Shields, M. B. (1995). Adsorption kinetics of asphaltenes at toluene/acid solution interface. *Fuel*, 74(10), 1475-1479.
38. Spiecker, P. M., Gawrys, K. L., & Kilpatrick, P. K. (2003). Aggregation and solubility behavior of asphaltenes and their subfractions. *Journal of Colloid and Interface Science*, 267(1), 178-193.
39. Andersen, S. I., & Birdi, K. S. (1991). Aggregation of asphaltenes as determined by calorimetry. *Journal of Colloid and Interface Science*, 142(2), 497-502.
40. Rodgers, R. P., Marshall, A. G., *Petroleomics: Advanced Characterization of Petroleum-Derived Materials by Fourier Transform Ion Cyclotron Resonance Mass Spectrometry (FT-ICR MS)*, Chapter 3, Asphaltenes, Heavy Oils, and Petroleomics, Editors: Mullins, O. C., Sheu, E. Y., Hammami, A., Marshall, A. G., Springer Science + Business Media, LLC, New York, 2007
41. Yarranton, H. W., "Asphaltene self-association", *J. Disp. Sci. Tech.*, 26 (1), 5-8, 2005.
42. Murgich, J., "Intermolecular forces in aggregates of asphaltenes and resins", *Petr. Sci. Technol.*, 20 (9&10), 983-997, 2002.
43. Rogel, E., "Simulation of interaction in asphaltene aggregates", *Energy Fuels*, 14 (3), 566-574, 2000.
44. Herzog, P., Tchoubar, D. and Espinat, D., Macrostructure of Asphaltene Dispersions by Small Angle X-ray Scattering, *Fuel*, 67(1988)245.
45. Xu, Y., Koga Y., Strausz, O.P., Characterization of Athabasca asphaltenes by small-angle x-ray scattering, *Fuel*, 74(1995)960-964.

46. Raveya, J.C., Ducouret, G., Espinat, D., Asphaltene macrostructure by small angle neutron scattering, *Fuel*, 67(1988)1560-1567.
47. Siddiqui, M. N., Ali, M. F., and Shirokoff, J. (2002). Use of X-ray Diffraction in Assessing the Aging Pattern of Asphalt Fractions. *Fuel*, 81(1), 51.
48. Gebresellasie, K., Lewis, J. C., & Shirokoff, J. (2013). X-ray spectral line shape analysis of asphalt binders. *Energy & Fuels*, 27(4), 2018-2024.
49. Lee, H., Dellatore, S. M., Miller, W. M., & Messersmith, P. B. (2007). Mussel-inspired surface chemistry for multifunctional coatings. *Science*, 318(5849), 426-430.
50. Anderson, D. A., & Bonaquist, R. (2012). NCHRP Report 709: Investigation of Short-term Laboratory Aging of Neat and Modified Asphalt Binders. Transportation Research Board of the National Academies, Washington, DC.
51. Bell. Summary Report on Aging of Asphalt Aggregate Systems, Transportation Research Board, 1989.
52. Ergun, S., & Tiensuu, V. (1959). Tetrahedral structures in amorphous carbons. *Acta Crystallographica*, 12(12), 1050-1051.
53. Shirokoff, J. W., Siddiqui, M. N., & Ali, M. F. (1997). Characterization of the structure of Saudi crude asphaltenes by X-ray diffraction. *Energy & Fuels*, 11(3), 561-565.
54. Sobien, H. (2012). The effect of mica on the aging of asphalt binder (Doctoral dissertation).

55. Cardoso, E. D. R., Braz, D., Motta, L. M. G., Barroso, R. C., & Lopes, R. T. Effect of The Weather in The Aging of Asphalts By XRD. In International Nuclear Atlantic Conference–INAC.
56. Alqahtani, H., Lewis, J. C., & Shirokoff, J. (2017, February). Modeling X-ray Line Shapes from Asphaltenes. In *Journal of Physics: Conference Series* (Vol. 810, No. 1, p. 012049). IOP Publishing.
57. Gebresellasie, K., Lewis, J. C., & Shirokoff, J. (2013). X-ray spectral line shape analysis of asphalt binders. *Energy & Fuels*, 27(4), 2018-2024.
58. Mullins, O. C., Sabbah, H., Eyssautier, J., Pomerantz, A. E., Barré, L., Andrews, A. B., ... & Lepkowicz, R. (2012). Advances in asphaltene science and the Yen–Mullins model. *Energy & Fuels*, 26(7), 3986-4003.
59. Kandhal, P. S., Roberts, F. L., Brown, E. R., Lee, D. Y., & Kennedy, T. W. (1996). *Hot mix asphalt materials, mixture design, and construction*. NAPA Education Foundation, Lanham, Md...
60. Specification, P. G. A. B. (2003). *Testing (Superpave Series No. 1)*. Asphalt Institute: Lexington, MA, USA. Asphalt Institute (Ed.). (2003). *Performance graded asphalt binder specification and testing (No. 1)*. Asphalt Institute.
61. Ghile, D. B. (2006). *Effects of nanoclay modification on the rheology of bitumen and on the performance of asphalt mixtures*. Delft, The Netherlands: Delft University of Technology
62. Zhen, M. F. Z. C. F. (2007). Performance & Modification Mechanism of Nano-CaCO<sub>3</sub> Modified Asphalt [J]. *Journal of Wuhan University of Technology (Transportation Science & Engineering)*, 1, 024.

63. Yu, J., Wang, L., Zeng, X., Wu, S., & Li, B. (2007). Effect of montmorillonite on properties of styrene-butadiene-styrene copolymer modified bitumen. *Polymer Engineering & Science*, 47(9), 1289-1295.
64. Yu, J., Zeng, X., Wu, S., Wang, L., & Liu, G. (2007). Preparation and properties of montmorillonite modified asphalts. *Materials Science and Engineering: A*, 447(1), 233-238.
65. <https://www.fhwa.dot.gov/publications/research/infrastructure/pavements/pccp/04122/03.cfm>
60. [http://www.fdot.gov/aviation/pdfs/pavement/fdot\\_field\\_manual\\_final\\_report.pdf](http://www.fdot.gov/aviation/pdfs/pavement/fdot_field_manual_final_report.pdf)
66. "Zanzotto, L.; Stastna, J. "Low-Temperature Stress Growth and Relaxation in Crack Sealing Materials" *Journal of Materials and Structures* (1998), 31(212), pp.551-554.
67. Li, Xue; Marasteanu, Mihai O. "Cohesive Modeling of Fracture in Asphalt Mixtures at Low Temperatures" *International Journal of Fracture* (2005), 136(1-4), pp.285-308.
68. You, Z., Mills-Beale, J., Foley, J. M., Roy, S., Odegard, G. M., Dai, Q., & Goh, S. W. (2011). Nanoclay-modified asphalt materials: Preparation and characterization. *Construction and Building Materials*, 25(2), 1072-1078.
69. Patricia Yee; Bill Aida; Hesp S. A. M. "Analysis of Premature Low Temperature Cracking in Three Ontario Pavement" *Journal of Transportation Research Board, Transportation Resources Record* (2006) 1962, pp.44-51.

70. Cullity, B. D., & Weymouth, J. W. (1957). Elements of X-ray Diffraction. *American Journal of Physics*, 25(6), 394-395.
71. Leng, Y. (2009). *Materials characterization: an introduction to microscopic and spectroscopic methods*. John Wiley & Sons.
72. Azaroff, L. V., & Buerger, M. J. (1953). *The Powder Method in X-ray Crystallography*.
73. Roberts, B. W., & Parrish, W. (1962). *International Tables for Crystallography, Vol. III*, edited by CH MacGillavry & GD Rieck
74. Gebresellasie, K., Shirokoff, J., and Lewis, J. C. (2012). Effect of X-ray LineSpectra Profile Fitting with Pearson VII, Pseudo-Voigt and Generalized Fermi Functions on Asphalt Binder Aromaticity and Crystallite Parameters. In *Journal of Physics: Conference Series* (Vol. 397, No. 1, p. 012069). IOP Publishing.
75. Saarinen, P. E., Kauppinen, J. K., & Partanen, J. O. (1995). New Method for Spectral line Shape Fitting and Critique on the Voigt line Shape Model. *Applied Spectroscopy*, 49(10), 1438-1453.
76. Inaba, K. (2008). X-ray thin-film measurement techniques. Overview. *Rigaku J*, 24(1).
77. Pecharsky, V. K., & Zavalij, P. Y. (2009). *Fundamentals of Powder Diffraction and Structural Characterization of Materials* (Vol. 69). New York: Springer.